

---

# A Three-Dimensional Continuum Simulation Method for Grain Boundary Motion Incorporating Dislocation Structure

Xiaoxue Qin · Luchan Zhang · Yang Xiang

**Abstract** We develop a continuum model for the dynamics of grain boundaries in three dimensions that incorporates the motion and reaction of the constituent dislocations. The continuum model is based on a simple representation of densities of curved dislocations on the grain boundary. Illposedness due to nonconvexity of the total energy is fixed by a numerical treatment based on a projection method that maintains the connectivity of the constituent dislocations. An efficient simulation method is developed, in which the critical but computationally expensive long-range interaction of dislocations is replaced by another projection formulation that maintains the constraint of equilibrium of the dislocation structure described by the Frank's formula. This continuum model is able to describe the grain boundary motion and grain rotation due to both coupling and sliding effects, to which the classical motion by mean curvature model does not apply. Comparisons with atomistic simulation results show that our continuum model is able to give excellent predictions of evolutions of low angle grain boundaries and their dislocation structures.

**Keywords** Grain boundary dynamics · Coupling and sliding motions · Dislocation dynamics · Frank's formula · Projection methods

## 1 Introduction

Grain boundaries are indispensable components in polycrystalline materials. The energy and dynamics of grain boundaries play essential roles in the me-

---

X. X. Qin

Department of Mathematics, Hong Kong University of Science and Technology, Clear Water Bay, Kowloon, Hong Kong. E-mail: maxqin@ust.hk

L. C. Zhang

College of Mathematics and Statistics, Shenzhen University, Shenzhen, 518060, China. Corresponding author. E-mail: zhanglc@szu.edu.cn

Y. Xiang

Department of Mathematics, Hong Kong University of Science and Technology, Clear Water Bay, Kowloon, Hong Kong. Corresponding author. E-mail: maxiang@ust.hk

chanical and plastic behaviors of the materials [39]. Most of the available continuum models for the dynamics of grain boundaries are based on the motion driven by the capillary force which is proportional to the local mean curvature of the grain boundary [39, 20, 33]. This motion is a process to reduce the interfacial energy  $\int_S \gamma dS$ , where  $S$  is the grain boundary and  $\gamma$  is the grain boundary energy density. If the energy density  $\gamma$  is fixed, the driving force given by variation of the total energy is in the normal direction of the grain boundary and is proportional to its mean curvature. There are many atomistic simulations and continuum models in the literature for the grain boundary motion driven by mean curvature, e.g., [7, 21, 22, 42, 25, 16, 46, 23, 30, 27, 47, 13, 26, 11, 12].

The decreasing of grain boundary energy density  $\gamma(\theta)$  can also reduce the total energy. For a low angle grain boundary, this implies the decreasing the misorientation angle  $\theta$ . In this case, the two grains on different sides of the grain boundary will rotate and cause a relatively rigid-body translation of the two grains along the boundary. This process is called sliding motion of grain boundaries [29, 37, 19, 24, 43, 15, 14].

There is a different type of grain boundary motion which is called coupling motion [28, 38, 6], in which the normal motion of the grain boundary induces a tangential motion proportionally. In the coupling motion, the energy density  $\gamma(\theta)$  can increase although the total energy  $\int_S \gamma dS$  is decreasing. Cahn and Taylor [6] proposed a unified theory for the coupling and sliding motions of the grain boundary and demonstrated the theory based on dislocation mechanisms for a circular low angle grain boundary in two dimensions. Especially, the coupling motion of the grain boundary is associated with dislocation conservation during the motion of the grain boundary. The Cahn-Taylor theory and mechanisms of motion and reaction of the constituent dislocations have been examined by atomistic simulations and experiments [38, 5, 32, 18, 41, 44, 31, 45, 36]. It has been shown in Ref. [35] by a dislocation model and experimental observations that conservation and annihilation of the constituent dislocations may lead to cancelation of the coupling and sliding motions of the grain boundary, leading to the classical motion by curvature. A continuum model has been developed based on the motion and reaction of the constituent dislocations for the dynamics of low angle grain boundaries in two dimensions [50]. Their model can describe both the coupling and sliding motions of low angle grain boundaries. Recently, they have proposed a more efficient numerical formulation [48]. A continuum model that generalizes the Cahn-Taylor theory based on mass transfer by diffusion confined on the grain boundary has been proposed [40], and numerical simulations based on this generalization were performed using the level set method [3]. Crystal plasticity models that include shear-coupled grain boundary motion in the phase field framework of Ref. [24] have been developed [1, 2], in which the geometric necessary dislocation (GND) tensor/lattice curvature tensor was used to approximate the actual dislocation distributions on the grain boundaries. All these continuum models are for grain boundaries in two dimensions.

There are only limited studies in the literature for the three-dimensional coupling and sliding motions of grain boundaries. Grain boundary motion and grain rotation in bcc and fcc bicrystals composed of a spherical grain embedded in a single crystal matrix were studied by using three-dimensional phase field crystal model [45] and amplitude expansion phase field crystal model [36], and properties of grain boundaries and their dislocation structures as the grain boundary evolves have been examined. Although these atomistic-level phase field crystal simulations are able to provide detailed information associated with the coupling and sliding motions of grain boundaries in three dimensions, three-dimensional continuum models of the dynamics of grain boundaries incorporating their dislocation structures are still desired for larger scale simulations.

In this paper, we generalize the two-dimensional continuum model for grain boundary dynamics in Ref. [50,48] to three dimensions, where grain boundaries and their constituent dislocations are curved in general. The three-dimensional continuum model for the dynamics of grain boundaries incorporates the motion and reaction of the constituent dislocations, and is able to describe both coupling and sliding motions of the grain boundaries, to which the classical motion by mean curvature model does not apply. The continuum model includes evolution equations for both the motion of the grain boundary and the evolution of dislocation structure on the grain boundary. The evolution of orientation-dependent continuous distributions of dislocation lines on the grain boundary is based on the simple representation using dislocation density potential functions [52]. This simple representation method also guarantees the continuity of the dislocation lines on the grain boundaries during the evolution. This continuum simulation framework for the distribution and dynamics of curves on curved surfaces can be applied more generally beyond the dynamics of dislocations and grain boundaries.

In a straightforward formulation of the continuum model, the variational force for the evolution of dislocations comes from a non-convex total energy, which leads to illposedness of the model. This problem is fixed by an alternative formulation with constraints, whose geometric meaning is to maintain the connectivity of dislocation lines. A numerical treatment based on a projection method is developed to solve the constrained evolution equations. The continuum model contains a long-range force in the form of singular integrals, whose evaluation is time-consuming especially in the three dimensional case. We generalize the projection method developed in two dimensional case [48] that replaces the long-range force by a constraint of the Frank's formula [17, 4,52] describing equilibrium of the long-range force. The projection procedure in three dimensional case can be solved, by generalizing the ideas in two dimensional case [48] with extra treatments to handle the Frank's formula in three dimensions and the connectivity of dislocations.

Using the obtained continuum model, we perform numerical simulations for the evolution of low angle grain boundaries by coupling and sliding motions, and compare the results with those of atomistic simulations using phase field crystal model [45] and amplitude expansion phase field crystal model [36] for

validation of our continuum model. We also explain the anisotropic motion observed in these atomistic simulations based on our continuum model.

This paper is organized as follows. In Sec. 2, we present a three dimensional continuum model for the evolution of grain boundaries with dislocation structures that is directly based on the simple representation of curved dislocation lines on curved grain boundaries and the associated energies and driving forces [52]. Illposedness of this formulation is discussed. In Sec. 3, in order to fix the illposedness problem, we present an alternative continuum formulation with constraints for the dynamics of grain boundaries in three dimensions, and propose a numerical treatment based on a projection method to solved the constrained evolution equations. In Sec. 4, we develop a more efficient formulation in which the computationally time-consuming long-range force is replaced by the constraint of the Frank's formula, and obtain an explicit solution formula of the projection procedure. Numerical simulations using our continuum model for the evolution of low angle grain boundaries by coupling and sliding motions are performed, and comparisons with the results of atomistic simulations using phase field crystal model [45] and amplitude expansion phase field crystal model [36] are made in Sec. 6.

## **2 Straightforward generalization to three dimensional model: Illposedness**

We have already developed two dimensional continuum model for the evolution of grain boundaries with dislocation structures that is able to describe the coupling and sliding motions of grain boundaries [50,48]. Recall that in two dimensions where the grain boundary is a curve and the dislocations are points, dislocation densities on the grain boundary can be described directly by scalar functions. However, in three dimensions where the grain boundary is a surface and dislocations are lines on the surface, scalar densities are not able to describe the distributions of orientation-dependent, connected dislocation lines. A simple representation using scalar functions (dislocation density potential functions) for the densities of connected, curved dislocation lines on curved grain boundaries and the associated energies and driving forces have been proposed in Ref. [52]. Using this representation, the orientation dependent dislocation densities are described based on surface gradient of the scalar dislocation density potential functions, instead of the scalar dislocation densities themselves in two dimension. This leads to illposedness in the straightforward generalization of the continuum dynamics model to three dimensions; see the discussion at the end of this section and more details in Theorem 1 in Sec. 5. In this section, we present this straightforward generalization of the continuum model to three dimensions. An alternative form of this formulation that fixes the illposedness will be presented in the next section.

Using the dislocation representation and dynamics formulation in Ref. [52], we have the following evolution equations of a grain boundary  $S$  and its dis-

location structure:

$$v_n = M_d \sum_{j=1}^J \frac{\|\nabla_S \eta_j\|}{\sum_{k=1}^J \|\nabla_S \eta_k\|} (\mathbf{f}_{\text{long}}^{(j)} + \mathbf{f}_{\text{local}}^{(j)}) \cdot \mathbf{n}, \quad (1)$$

$$\frac{\partial \eta_j}{\partial t} = -M_d \mathbf{f}_{\text{long}}^{(j)} \cdot \nabla_S \eta_j - M_\eta \mathbf{f}_{\text{local}}^{(j)} \cdot \frac{\nabla_S \eta_j}{\|\nabla_S \eta_j\|}, \quad j = 1, 2, \dots, J. \quad (2)$$

Eq. (1) governs the evolution of the grain boundary, and Eq. (2) describes evolution of the constituent dislocations on the grain boundary. The first term on the right-hand side of Eq. (2) describes the motion of the constituent dislocations on the grain boundaries, and the second term models the change of dislocations due to dislocation reaction. Here it is assumed that there are  $J$  arrays of dislocations with Burgers vectors  $\mathbf{b}^{(j)}$ ,  $j = 1, 2, \dots, J$ , respectively, on the grain boundary, and they are described by the dislocation density potential functions  $\eta_j$ ,  $j = 1, 2, \dots, J$ , respectively. In these evolution equations,  $M_d > 0$  is the mobility of the constituent dislocations, and  $M_\eta > 0$  is the mobility associated with dislocation reaction.

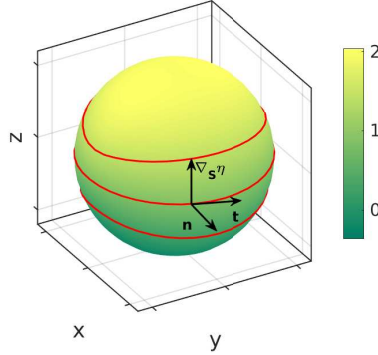


**Fig. 1** A dislocation density potential function  $\eta$  defined on a grain boundary  $S$ . Its integer-value contour lines represent the array of dislocations with the same Burgers vector.  $\mathbf{n}$  is the unit normal vector of the grain boundary, and  $\mathbf{t}$  is the local dislocation line direction.

For a dislocation density potential function  $\eta$  defined on a grain boundary  $S$ , the constituent dislocations of Burgers vector  $\mathbf{b}$  are given by the contour lines of  $\eta$ :  $\eta = i$ , for integer  $i$ . See Fig. 1 for an example of dislocation structure on a spherical grain boundary and  $\eta$  defined on it. From the dislocation density potential function  $\eta$ , the inter-dislocation distance  $D$  can be calculated by  $D = \frac{1}{\|\nabla_S \eta\|}$ , and the dislocation direction is given by  $\mathbf{t} = \frac{\nabla_S \eta \times \mathbf{n}}{\|\nabla_S \eta\|}$ , where  $\nabla_S \eta$  is the surface gradient of  $\eta$  on  $S$ :  $\nabla_S \eta = (\nabla - \mathbf{n}(\mathbf{n} \cdot \nabla))\eta$ , and  $\mathbf{n}$  is the unit normal vector of the grain boundary. Multiple dislocation density potential functions are used for dislocations with different Burgers vectors.

From the physical meaning, we always have  $\|\nabla_S \eta\| \leq \frac{1}{b}$ , meaning that the inter-dislocation distance  $D \geq b$ .

The continuum formulation of the total energy is

$$E_{\text{tot}} = E_{\text{long}} + E_{\text{local}}, \quad (3)$$

$$E_{\text{long}} = \frac{1}{2} \sum_{i=1}^J \sum_{j=1}^J \int_S dS_i \int_S dS_j \left[ \frac{\mu}{4\pi} \frac{(\nabla_S \eta_i \times \mathbf{n}_i \cdot \mathbf{b}^{(i)})(\nabla_S \eta_j \times \mathbf{n}_j \cdot \mathbf{b}^{(j)})}{r_{ij}} \right. \\ \left. - \frac{\mu}{2\pi} \frac{(\nabla_S \eta_i \times \mathbf{n}_i) \times (\nabla_S \eta_j \times \mathbf{n}_j) \cdot (\mathbf{b}^{(i)} \times \mathbf{b}^{(j)})}{r_{ij}} \right. \\ \left. + \frac{\mu}{4\pi(1-\nu)} (\nabla_S \eta_i \times \mathbf{n}_i \cdot \mathbf{b}^{(i)}) \cdot (\nabla \otimes \nabla r_{ij}) \cdot (\nabla_S \eta_j \times \mathbf{n}_j \cdot \mathbf{b}^{(j)}) \right], \quad (4)$$

$$E_{\text{local}} = \int_S \gamma_{\text{gb}} dS, \quad (5)$$

$$\gamma_{\text{gb}} = \sum_{j=1}^J \frac{\mu(b^{(j)})^2}{4\pi(1-\nu)} \left( 1 - \nu \frac{(\nabla_S \eta_j \times \mathbf{n} \cdot \mathbf{b}^{(j)})^2}{(b^{(j)})^2 \|\nabla_S \eta_j\|^2} \right) \|\nabla_S \eta_j\| \log \frac{1}{r_g \|\nabla_S \eta_j\|}. \quad (6)$$

Here  $E_{\text{long}}$  is the long-range interaction energy of dislocations, and  $E_{\text{local}}$  is the local dislocation line energy with energy density  $\gamma_{\text{gb}}$ . In the formulation of  $E_{\text{long}}$  in Eq. (4),  $r_{ij} = \|\mathbf{X}_i - \mathbf{X}_j\|$ , where  $\mathbf{X}_i$  and  $\mathbf{X}_j$  are the points varying on the grain boundary  $S$  and are associated with the surface integral  $dS_i$  and  $dS_j$ , respectively.  $\mathbf{n}_j$  is the normal direction of the surface  $S$  associated with the surface integral  $dS_j$ , notation  $\otimes$  is the tensor product operator, the gradient in the term  $\nabla \otimes \nabla r_{ij}$  is taken with respect to  $\mathbf{X}_i$ , and  $b^{(j)} = \|\mathbf{b}^{(j)}\|$ . The elastic constants  $\mu$  is the shear modulus and  $\nu$  is the Poisson's ratio. The parameter  $r_g$  in  $\gamma_{\text{gb}}$  in Eq. (6) depends on the size and energy of the dislocation core, and is of the order of  $b$ .

The driving forces for the dynamics of the grain boundary and the dislocation structure are associated with the variations of the total energy. In the grain boundary dynamics equations (1) and (2),  $\mathbf{f}_{\text{long}}^{(j)}$  is the continuum long-range force, and  $\mathbf{f}_{\text{local}}^{(j)}$  the local force on the  $\mathbf{b}^{(j)}$ -dislocations. These forces have

the following formulations:

$$\mathbf{f}_{\text{long}}^{(j)} = (\boldsymbol{\sigma}^{\text{tot}} \cdot \mathbf{b}^{(j)}) \times \left( \frac{\nabla_S \eta_j}{\|\nabla_S \eta_j\|} \times \mathbf{n} \right), \quad (7)$$

$$\begin{aligned} \boldsymbol{\sigma}^{\text{tot}} = & \sum_{j=1}^J \frac{\mu}{4\pi} \int_S \left[ \left( \nabla \frac{1}{r} \times \mathbf{b}^{(j)} \right) \otimes (\nabla_S \eta_j \times \mathbf{n}) + (\nabla_S \eta_j \times \mathbf{n}) \times \left( \nabla \frac{1}{r} \times \mathbf{b}^{(j)} \right) \right. \\ & \left. + \frac{1}{1-\nu} \left( \mathbf{b}^{(j)} \times (\nabla_S \eta_j \times \mathbf{n}) \cdot \nabla \right) (\nabla \otimes \nabla - I\Delta)r \right] dS + \boldsymbol{\sigma}^{\text{app}}, \quad (8) \end{aligned}$$

$$\begin{aligned} \mathbf{f}_{\text{local}}^{(j)} = & \frac{\mu}{4\pi(1-\nu)} \kappa_d \left[ (1+\nu)(b_t^{(j)})^2 + (1-2\nu)(b_N^{(j)})^2 + (b_B^{(j)})^2 \right] \log \frac{1}{r_g \|\nabla_S \eta_j\|} \mathbf{n}_d^{(j)} \\ & - \frac{\mu\nu}{2\pi(1-\nu)} \kappa_d b_N^{(j)} b_B^{(j)} \mathbf{t}^{(j)} \times \mathbf{n}_d^{(j)} + \frac{\mu}{4\pi(1-\nu)} \kappa_p^{(j)} \left[ (b^{(j)})^2 - \nu(b_t^{(j)})^2 \right] \mathbf{n}_p^{(j)} \\ & + \frac{\mu}{4\pi(1-\nu)} \left[ (b^{(j)})^2 - \nu(b_t^{(j)})^2 \right] \frac{(\nabla_S \nabla_S \eta_j) \cdot \nabla_S \eta_j}{\|\nabla_S \eta_j\|^2}. \quad (9) \end{aligned}$$

Here  $\boldsymbol{\sigma}^{\text{tot}}$  is the total stress field, which includes the long-range stress field generated by the dislocation arrays on  $S$ , i.e., the first integral term, and the other stress fields  $\boldsymbol{\sigma}^{\text{app}}$ , and in this formulation of  $\boldsymbol{\sigma}^{\text{tot}}$ ,  $r = \|\mathbf{X} - \mathbf{X}_S\|$  with points  $\mathbf{X}_S$  varying on the grain boundary  $S$  and  $\nabla_S \eta_j$  and  $\mathbf{n}$  being evaluated at  $\mathbf{X}_S$ . In the local force  $\mathbf{f}_{\text{local}}^{(j)}$  in Eq. (9),  $\kappa_d$  is the curvature of dislocation line,  $\mathbf{n}_d$  is the normal direction of dislocation,  $\kappa_p$  and  $\mathbf{n}_p$  are the curvature and normal direction of the curve on  $S$  that is normal to the location dislocation, respectively, and  $\kappa_d \mathbf{n}_d = (\nabla_S \mathbf{t}) \cdot \mathbf{t} = \nabla_S \left( \frac{\nabla_S \eta_j}{\|\nabla_S \eta_j\|} \times \mathbf{n} \right) \cdot \left( \frac{\nabla_S \eta_j}{\|\nabla_S \eta_j\|} \times \mathbf{n} \right)$ ,  $\kappa_p \mathbf{n}_p = \left( \nabla_S \frac{\nabla_S \eta_j}{\|\nabla_S \eta_j\|} \right) \cdot \frac{\nabla_S \eta_j}{\|\nabla_S \eta_j\|}$ ,  $b_t = \mathbf{b} \cdot \mathbf{t}$ ,  $b_N = \mathbf{b} \cdot \mathbf{n}_d$ ,  $b_B = \mathbf{b} \cdot (\mathbf{t} \times \mathbf{n}_d)$ .

### Illposedness of this formulation

Unfortunately, Eqs. (1) and (2) do not form a wellposed formulation. Especially, the evolution equation of dislocation structure in (2) is illposed. In fact, Eq. (2) is a second order evolution equation of  $\eta_j$ , which is determined by the second term  $-M_\eta \mathbf{f}_{\text{local}}^{(j)} \cdot \frac{\nabla_S \eta_j}{\|\nabla_S \eta_j\|} = -M_\eta \frac{\delta E_{\text{local}}}{\delta \eta_j}$ , where  $\mathbf{f}_{\text{local}}^{(j)}$  is given in Eq. (9). Note that  $\kappa_d$ ,  $\mathbf{n}_d$  and  $\kappa_p$ ,  $\mathbf{n}_p$  in  $\mathbf{f}_{\text{local}}^{(j)}$  are all expressed in terms of second partial derivatives of  $\eta_j$ . However, the energy density  $\gamma_{\text{gb}}$  of the local energy  $E_{\text{local}}$  in (5) and (6) is not convex as a function of  $\nabla_S \eta_j$ . This nonconvexity leads to an illposed formulation when using the gradient flow  $\frac{\partial \eta_j}{\partial t} = -M_\eta \frac{\delta E_{\text{local}}}{\delta \eta_j} = -M_\eta \mathbf{f}_{\text{local}}^{(j)} \cdot \frac{\nabla_S \eta_j}{\|\nabla_S \eta_j\|}$  for the evolution of  $\eta_j$ . This can be understood as follows. Neglecting the orientation dependence factor, the contribution of  $\eta_j$  in the energy density  $\gamma_{\text{gb}}$  is essentially  $-\|\nabla_S \eta_j\| \log \|\nabla_S \eta_j\|$ , which is a concave function of  $\|\nabla_S \eta_j\|$ . As a result, the gradient flow gives a backward-diffusion like illposed evolution equation of  $\eta_j$ . See Theorem 1 in Sec. 5 for detail of the proof. Therefore, the continuum model in Eqs. (1) and (2) cannot be used directly to simulate the evolution of the grain boundary and its dislocation structure.

### 3 Continuum model for grain boundary dynamics in three dimensions

In this section, we present a continuum model for the dynamics of grain boundaries in three dimensions incorporating the coupling and sliding motions, which fixes the illposedness problem in the formulation in Eqs. (1) and (2).

In order to obtain a gradient flow formulation that avoids the above discussed illposedness for the evolution of the dislocation structure represented by dislocation density potential functions  $\eta_j$ ,  $j = 1, 2, \dots, J$ , we use the components of  $\nabla_S \eta_j$  as independent variables instead of  $\eta_j$  itself in the evolution equation of dislocation structure. That is, when the grain boundary  $S$  is expressed by  $\mathbf{r}(u, v)$ , where  $(u, v)$  is an orthogonal parametrization with  $\|\mathbf{r}_u\| = \|\mathbf{r}_v\| = 1$ , we have

$$\nabla_S \eta_j = \eta_{ju} \mathbf{r}_u + \eta_{jv} \mathbf{r}_v, \quad (10)$$

where  $\eta_{ju}$  and  $\eta_{jv}$  are partial derivatives of  $\eta_j$  with respect to  $u$  and  $v$ , and  $\mathbf{r}_u$  and  $\mathbf{r}_v$  are partial derivatives of  $\mathbf{r}$  with respect to  $u$  and  $v$ . We use  $\eta_{ju}$  and  $\eta_{jv}$  as independent variables for the evolution of dislocation structure. Gradient flow based on variations of the local energy taken with respect to  $\eta_{ju}$  and  $\eta_{jv}$  gives:

$$\frac{\partial \eta_{ju}}{\partial t} = -M_r \frac{\delta E_{\text{local}}}{\delta \eta_{ju}} = -M_r \frac{\partial \gamma_{\text{gb}}}{\partial \eta_{ju}}, \quad (11)$$

$$\frac{\partial \eta_{jv}}{\partial t} = -M_r \frac{\delta E_{\text{local}}}{\delta \eta_{jv}} = -M_r \frac{\partial \gamma_{\text{gb}}}{\partial \eta_{jv}}, \quad (12)$$

where  $M_r > 0$ . Noticing that the local energy density  $\gamma_{\text{gb}}$  is a function of  $\nabla_S \eta_j = \eta_{ju} \mathbf{r}_u + \eta_{jv} \mathbf{r}_v$ , the gradient flow equations in (11) and (12) are ODEs of  $\eta_{ju}$  and  $\eta_{jv}$  with respect to time  $t$ . For this ODE system, we have the standard local existence for the solution [10]. As a result, illposedness due to the backward-diffusion like PDEs of  $\eta_j$  in the original formulation is avoided.

However, this alternative formulation leads to a new problem that as partial derivatives of the same function,  $\eta_{ju}$  and  $\eta_{jv}$  are not independent. In fact, they are related by  $\frac{\partial \eta_{ju}}{\partial v} - \frac{\partial \eta_{jv}}{\partial u} = 0$ . Recalling that dislocations are contour lines of the functions  $\{\eta_j\}$  on the grain boundary, the physical meaning of these relations is that the dislocations are connected lines on the grain boundary, i.e., there is no dislocation source/sink at any point on the grain boundary.<sup>1</sup> In order to fix this new problem, we include these relations of  $\eta_{ju}$  and  $\eta_{jv}$ ,  $j = 1, 2, \dots, J$ , as constraints in the continuum model. Using these treatments and combining the contribution from the long-range energy, the continuum formulation can be rewritten as:

#### Continuum model with constraints

<sup>1</sup> In fact, the net dislocation flux across the boundary of any region  $\Omega$  on the grain boundary is  $\int_{\partial\Omega} \nabla_S \eta_j \cdot d\mathbf{r} = \int_{\Omega} \left( \frac{\partial \eta_{jv}}{\partial u} - \frac{\partial \eta_{ju}}{\partial v} \right) dudv = 0$  using this condition.



$$v_n = M_d \sum_{j=1}^J \frac{\|\nabla_S \eta_j\|}{\sum_{k=1}^J \|\nabla_S \eta_k\|} (\mathbf{f}_{\text{long}}^{(j)} + \mathbf{f}_{\text{local}}^{(j)}) \cdot \mathbf{n}, \quad (13)$$

$$\frac{\partial \eta_{ju}}{\partial t} = -M_d \frac{\partial}{\partial u} (\mathbf{f}_{\text{long}}^{(j)} \cdot \nabla_S \eta_j) - M_r \frac{\partial \gamma_{\text{gb}}}{\partial \eta_{ju}}, \quad (14)$$

$$\frac{\partial \eta_{jv}}{\partial t} = -M_d \frac{\partial}{\partial v} (\mathbf{f}_{\text{long}}^{(j)} \cdot \nabla_S \eta_j) - M_r \frac{\partial \gamma_{\text{gb}}}{\partial \eta_{jv}}, \quad (15)$$

$$\text{subject to } \frac{\partial \eta_{ju}}{\partial v} - \frac{\partial \eta_{jv}}{\partial u} = 0. \quad (16)$$

Here  $M_r > 0$  is the mobility associated with dislocation reaction based on the energy variations with respect to  $\eta_{ju}$  and  $\eta_{jv}$ .

Numerically, we implement the constraint in Eq. (16) using a projection method similar to that for fluid dynamics problems [8]. Since evolution of  $\eta_{ju}$  and  $\eta_{jv}$  due to the first term in Eqs. (14) and (15) satisfies the constraint, we only need to focus on the deviation from the constraint due to the second terms therein.

Recall that the second terms in the evolution of  $\eta_{ju}$  and  $\eta_{jv}$  in Eqs. (14) and (15) come from the gradient flow of the local energy  $E_{\text{local}} = \int_S \gamma_{\text{gb}} dS$ . In order to implement the constraint in Eq. (16), we introduce a Lagrangian function:

$$L = \int_S \left( \gamma_{\text{gb}} + \sum_{j=1}^J \lambda_j \left( \frac{\partial \eta_{ju}}{\partial v} - \frac{\partial \eta_{jv}}{\partial u} \right) \right) dS, \quad (17)$$

where  $\lambda_j$ ,  $j = 1, 2, \dots, J$ , are Lagrange multipliers associated with the constraints. Using the Lagrangian function  $L$  instead of  $E_{\text{local}}$  in the gradient flow, the evolution of dislocation structure in Eqs. (14) and (15) becomes

$$\frac{\partial \eta_{ju}}{\partial t} = -M_d \frac{\partial}{\partial u} (\mathbf{f}_{\text{long}}^{(j)} \cdot \nabla_S \eta_j) - M_r \frac{\partial \gamma_{\text{gb}}}{\partial \eta_{ju}} + \frac{\partial \lambda_j}{\partial v}, \quad (18)$$

$$\frac{\partial \eta_{jv}}{\partial t} = -M_d \frac{\partial}{\partial v} (\mathbf{f}_{\text{long}}^{(j)} \cdot \nabla_S \eta_j) - M_r \frac{\partial \gamma_{\text{gb}}}{\partial \eta_{jv}} - \frac{\partial \lambda_j}{\partial u}. \quad (19)$$

Here the coefficients of  $\frac{\partial \lambda_j}{\partial v}$  and  $\frac{\partial \lambda_j}{\partial u}$  in these equations are set to be 1.

During the evolution in the time step from  $t_n$  to  $t_{n+1} = t_n + \delta t$ , we separate the evolution of  $\eta_{ju}$  and  $\eta_{jv}$  into two steps:

$$\eta_{ju}^* = \eta_{ju}^n - \left[ M_d \frac{\partial}{\partial u} (\mathbf{f}_{\text{long}}^{(j)} \cdot \nabla_S \eta_j) + M_r \frac{\partial \gamma_{\text{gb}}}{\partial \eta_{ju}} \right]_{t_n} \cdot \delta t, \quad (20)$$

$$\eta_{jv}^* = \eta_{jv}^n - \left[ M_d \frac{\partial}{\partial v} (\mathbf{f}_{\text{long}}^{(j)} \cdot \nabla_S \eta_j) + M_r \frac{\partial \gamma_{\text{gb}}}{\partial \eta_{jv}} \right]_{t_n} \cdot \delta t, \quad (21)$$

$$\eta_{ju}^{n+1} = \eta_{ju}^* + \frac{\partial \lambda_j^{n+1}}{\partial v} \delta t, \quad \eta_{jv}^{n+1} = \eta_{jv}^* - \frac{\partial \lambda_j^{n+1}}{\partial u} \delta t. \quad (22)$$

In order to satisfy the constraint  $\frac{\partial \eta_{ju}^{n+1}}{\partial v} - \frac{\partial \eta_{jv}^{n+1}}{\partial u} = 0$ , using Eq. (22), we have the formula for updating  $\lambda_j$ :

$$\Delta \lambda_j^{n+1} = \frac{1}{\delta t} \left( \frac{\partial \eta_{jv}^*}{\partial u} - \frac{\partial \eta_{ju}^*}{\partial v} \right), \quad (23)$$

where  $\Delta$  is the Laplace operator. This Poisson equation for  $\lambda_j^{n+1}$  can be solved using a finite difference method. See Theorem 2 in Sec. 5 for the property of this projection method.

The numerical algorithm for solving the continuum model with constraints is summarized as follows:

### Numerical algorithm for solving constrained evolution

From  $t_n$  to  $t_{n+1} = t_n + \delta t$ ,

$$\begin{aligned} \mathbf{r}^{n+1} &= \mathbf{r}^n + v_n \mathbf{n} \Big|_{t_n} \cdot \delta t, \\ \eta_{ju}^* &= \eta_{ju}^n - \left[ M_d \frac{\partial}{\partial u} (\mathbf{f}_{\text{long}}^{(j)} \cdot \nabla_S \eta_j) + M_r \frac{\partial \gamma_{\text{gb}}}{\partial \eta_{ju}} \right]_{t_n} \cdot \delta t, \\ \eta_{jv}^* &= \eta_{jv}^n - \left[ M_d \frac{\partial}{\partial v} (\mathbf{f}_{\text{long}}^{(j)} \cdot \nabla_S \eta_j) + M_r \frac{\partial \gamma_{\text{gb}}}{\partial \eta_{jv}} \right]_{t_n} \cdot \delta t, \\ \Delta \lambda_j^{n+1} &= \frac{1}{\delta t} \left( \frac{\partial \eta_{jv}^*}{\partial u} - \frac{\partial \eta_{ju}^*}{\partial v} \right), \\ \eta_{ju}^{n+1} &= \eta_{ju}^* + \frac{\partial \lambda_j^{n+1}}{\partial v} \delta t, \quad \eta_{jv}^{n+1} = \eta_{jv}^* - \frac{\partial \lambda_j^{n+1}}{\partial u} \delta t. \end{aligned}$$

### 4 Continuum model without long-range force

The continuum model given by Eqs. (13)–(16) contains the long-range elastic force  $\mathbf{f}_{\text{long}}^{(j)}$  (given in Eqs. (7) and (8)), which is a singular integral over the entire grain boundary surface. Numerically, computation of such long-range force with reasonable accuracy is complicated and time-consuming even in two-dimensional cases [50, 48]. It has been shown in two-dimensional cases [48] by comparison with discrete dislocation dynamics simulations that the long-range interaction between the grain boundary dislocations is so strong that an equilibrium state described by the Frank's formula [17, 4, 52] is quickly reached during the evolution of the grain boundary. Here we follow the assumption made in two-dimensional case that the Frank's formula always holds during the evolution of the grain boundary [48]. This leads to a new three dimensional formulation without long-range force:

#### Continuum model without long-range force

$$v_n = M_d \sum_{j=1}^J \frac{\|\nabla_S \eta_j\|}{\sum_{k=1}^J \|\nabla_S \eta_k\|} \mathbf{f}_{\text{local}}^{(j)} \cdot \mathbf{n}, \quad (24)$$

$$\frac{\partial \eta_{ju}}{\partial t} = -M_r \frac{\partial \gamma_{\text{gb}}}{\partial \eta_{ju}}, \quad \frac{\partial \eta_{jv}}{\partial t} = -M_r \frac{\partial \gamma_{\text{gb}}}{\partial \eta_{jv}}, \quad (25)$$

$$\text{subject to } \frac{\partial \eta_{ju}}{\partial v} - \frac{\partial \eta_{jv}}{\partial u} = 0, \quad (26)$$

$$\mathbf{h} = \theta (\mathbf{V} \times \mathbf{a}) - \sum_{j=1}^J \mathbf{b}^{(j)} (\nabla_S \eta_j \cdot \mathbf{V}) = \mathbf{0}. \quad (27)$$

Here, the constraint (27) is the Frank's formula that governs the equilibrium dislocation structure on a grain boundary [17, 4, 52], in which  $\theta$  is the misorientation angle of the grain boundary and is a constant over the grain

boundary at any fixed time,  $\mathbf{a}$  is the rotation axis, and  $\mathbf{V}$  is any vector in the grain boundary's tangent plane. For a planar grain boundary, the Frank's formula holds if and only if the long-range elastic fields generated by the grain boundary cancel out [17, 4]. It has been shown in Ref. [52] that this equivalence also holds for a curved grain boundary.

Numerically, the constraint of Frank's formula in Eq. (27) can also be implemented using a projection method, i.e., projecting in each time step the virtual evolution result without the constraint of the Frank's formula to a nearby configuration that satisfies the Frank's formula. This is a separate numerical treatment in addition to the project method discussed in the previous section for handling the constraint in (26) for continuity of dislocation lines.

Specifically, in the evolution from  $t_n$  to  $t_{n+1} = t_n + \delta t$ , in the virtual evolution of the grain boundary without the constraint of Frank's formulation in (27), we have

$$\mathbf{r}^* = \mathbf{r}^n + \mathbf{v}^* \delta t, \quad (28)$$

$$\mathbf{v}^* = v_n, \quad (29)$$

where  $\mathbf{v}^* = (v_1^*, v_2^*, v_3^*)$  is the virtual velocity due to the local force without the constraint, i.e.,  $v_n$  in Eq. (24). Evolution of dislocation structure represented by  $\eta_j$ 's remains the same as that given in the previous section.

In the projection step, the virtual profile of the grain boundary  $\mathbf{r}^*$  is projected to a nearby configuration that satisfies the Frank's formula (27). Note that misorientation angle  $\theta$  is needed in (27) at time  $t_{n+1}$ . We calculate the misorientation angle  $\theta$  during the evolution by

$$\theta = \frac{1}{S_A} \int_S \sum_{j=1}^J \frac{(\eta_{ju} + \eta_{jv})(\mathbf{r}_u + \mathbf{r}_v) \times \mathbf{a} \cdot \mathbf{b}^{(j)}}{\|(\mathbf{r}_u + \mathbf{r}_v) \times \mathbf{a}\|^2} dS. \quad (30)$$

where  $S_A$  is the area of the grain boundary  $S$  that can be calculated by  $S_A = \int_S \|\mathbf{r}_u \times \mathbf{r}_v\| dudv$ . This formulation of  $\theta$  is obtained by taking average of the vector equation (27) in the  $\mathbf{r}_u$  and  $\mathbf{r}_v$  directions; see Appendix for details of the derivation. We calculate  $\theta^{n+1}$  using this formula based on the virtual evolution result of  $\mathbf{r}^*$ , i.e.,  $\theta^{n+1} = \theta(\mathbf{r}_u^*, \mathbf{r}_v^*, \eta_{ju}^{n+1}, \eta_{jv}^{n+1})$ . This means that we assume that the value of  $\theta$  does not change in the projection step. Based on this obtained  $\theta^{n+1}$ , the actual grain boundary velocity  $\mathbf{v}$  is obtained by projection of the virtual configuration of the grain boundary  $\mathbf{r}^*$  to a state  $\mathbf{r}^{n+1}$  that satisfies the constraint of Frank's formula (27).

This projection procedure has been validated in the two dimensional case by comparisons with the full evolution with the long-range force and discrete dislocation dynamics simulation, and explicit formula of the velocity after projection has been obtained in the two dimensional case [48]. Here we generalize the projection procedure to three dimensional case, based on the formulation of misorientation angle  $\theta$  in the three dimensional case established in Eq. (30). The projection procedure in three dimensional case here can also be solved similarly as in the two dimensional case, with extra treatments to handle the Frank's formula in three dimensions and connectivity of dislocations.

Now we solve the projection procedure in three dimensional case. Without loss of generality, suppose that the rotation axis is in the  $+z$  direction, i.e.,  $\mathbf{a} = (0, 0, 1)$ .

Suppose that the grain boundary velocity is  $\mathbf{v}$ , and the Frank's formula (27) holds at the time  $t_n$ . After a small time step  $\delta t$ , if the Frank's formula still holds at  $t_{n+1} = t_n + \delta t$ , we have

$$(\delta\theta\mathbf{r}_u + \theta\delta t\mathbf{v}_u) \times \mathbf{a} - \sum_{j=1}^J \mathbf{b}^{(j)} \delta\eta_{ju} = 0, \quad (31)$$

$$(\delta\theta\mathbf{r}_v + \theta\delta t\mathbf{v}_v) \times \mathbf{a} - \sum_{j=1}^J \mathbf{b}^{(j)} \delta\eta_{jv} = 0. \quad (32)$$

Here we have used  $\delta\mathbf{r}_u = \delta t\mathbf{v}_u$  and  $\delta\mathbf{r}_v = \delta t\mathbf{v}_v$ , where  $\mathbf{v}_u = \frac{\partial\mathbf{v}}{\partial u}$  and  $\mathbf{v}_v = \frac{\partial\mathbf{v}}{\partial v}$ .

Integrating Eq. (31) with respect to  $u$ , and Eq. (32) with respect to  $v$ , we have

$$\begin{aligned} & (\delta\theta\mathbf{r}(u, v) + \theta\delta t\mathbf{v}(u, v)) \times \mathbf{a} - \sum_{j=1}^J \mathbf{b}^{(j)} \delta\eta_j(u, v) \\ &= (\delta\theta\mathbf{r}(0, v) + \theta\delta t\mathbf{v}(0, v)) \times \mathbf{a} - \sum_{j=1}^J \mathbf{b}^{(j)} \delta\eta_j(0, v), \end{aligned} \quad (33)$$

$$\begin{aligned} & (\delta\theta\mathbf{r}(u, v) + \theta\delta t\mathbf{v}(u, v)) \times \mathbf{a} - \sum_{j=1}^J \mathbf{b}^{(j)} \delta\eta_j(u, v) \\ &= (\delta\theta\mathbf{r}(u, 0) + \theta\delta t\mathbf{v}(u, 0)) \times \mathbf{a} - \sum_{j=1}^J \mathbf{b}^{(j)} \delta\eta_j(u, 0). \end{aligned} \quad (34)$$

Notice that the left-hand sides of Eqs. (33) and (34) are equal, whereas the right-hand side of Eq. (33) depends only on  $v$  and the right-hand side of Eq. (34) depends only on  $u$ . Thus the right-hand sides of Eqs. (33) and (34) must equal to the same constant independent of  $u$  and  $v$ , denoted by  $\mathbf{C} = (c_1, c_2, c_3)$ . That is,

$$(\delta\theta\mathbf{r}(u, v) + \theta\delta t\mathbf{v}(u, v)) \times \mathbf{a} - \sum_{j=1}^J \mathbf{b}^{(j)} \delta\eta_j(u, v) = \mathbf{C}. \quad (35)$$

We want to solve for the actual velocity  $\mathbf{v} = (v_1, v_2, v_3)$  such that the above vector equation holds. Since  $\mathbf{a} = (0, 0, 1)$ , the first two equations in (35) give

$$v_1 = -\frac{\delta\theta}{\theta\delta t}(x - c_1) - \frac{1}{\theta} \sum_{j=1}^J b_2^{(j)} \frac{\delta\eta_j}{\delta t}, \quad (36)$$

$$v_2 = -\frac{\delta\theta}{\theta\delta t}(y - c_2) + \frac{1}{\theta} \sum_{j=1}^J b_1^{(j)} \frac{\delta\eta_j}{\delta t}. \quad (37)$$

Note that in the projection procedure, we essentially adjust the local value of  $\theta$  determined by the Frank's formula in Eq. (27) to achieve a uniform misorientation angle  $\theta$  over the entire grain boundary. This procedure should not lead to additional rigid translation of the grain boundary. The two constants  $c_1$  and  $c_2$  in the projected velocity formula in Eqs. (36) and (37) can be determined by this condition. For some symmetric configuration of the grain boundary, e.g., when the top point of the grain boundary in the  $+z$  direction always has a velocity in the  $z$  direction due to some symmetry, we set the  $z$  axis passing through that point, i.e., that point is  $\mathbf{r} = (0, 0, z)$  during the evolution. In this case, at that point, we have  $(\delta\theta\mathbf{r} + \theta\delta t\mathbf{v}) \times \mathbf{a} = \mathbf{0}$ , and we set  $\eta_j = 0$ ,  $j = 1, 2, \dots, J$ , at that point. Thus, we have  $c_1 = c_2 = 0$ . Eqs. (36) and (37) actually hold in the continuum model, i.e.,  $v_1 = -\frac{1}{\theta}\frac{d\theta}{dt}(x - c_1) - \frac{1}{\theta}\sum_{j=1}^J b_2^{(j)}\frac{d\eta_j}{dt}$  and  $v_2 = -\frac{1}{\theta}\frac{d\theta}{dt}(y - c_2) + \frac{1}{\theta}\sum_{j=1}^J b_1^{(j)}\frac{d\eta_j}{dt}$ , by letting  $\delta t \rightarrow 0$ .

The condition in Eq. (35) does not impose any restriction on the velocity in the direction of the rotation axis, i.e., the  $z$  direction. Thus we simply keep the  $z$ -component  $v_3 = v_3^*$ , where  $\mathbf{v}^* = (v_1^*, v_2^*, v_3^*)$  is the virtual velocity in Eq. (29) without the constraint of the Frank's formula.

In summary, combining with the algorithm to maintain the dislocation continuity presented in previous section, we have the following efficient numerical algorithm without calculation of the long-range force:

### Numerical Algorithm

From  $t_n$  to  $t_{n+1} = t_n + \delta t$ ,

$$\mathbf{v}^* = \left( M_d \sum_{j=1}^J \frac{\|\nabla S \eta_j\|}{\sum_{k=1}^J \|\nabla S \eta_k\|} \mathbf{f}_{\text{local}}^{(j)} \cdot \mathbf{n} \right) \mathbf{n}, \quad (38)$$

$$\mathbf{r}^* = \mathbf{r}^n + \mathbf{v}^* \delta t, \quad (39)$$

$$\eta_{ju}^* = \eta_{ju}^n - M_r \left. \frac{\partial \gamma_{\text{gb}}}{\partial \eta_{ju}} \right|_{t_n} \delta t, \quad \eta_{jv}^* = \eta_{jv}^n - M_r \left. \frac{\partial \gamma_{\text{gb}}}{\partial \eta_{jv}} \right|_{t_n} \delta t, \quad (40)$$

$$\Delta \lambda_j^{n+1} = \frac{1}{\delta t} \left( \frac{\partial \eta_{jv}^*}{\partial u} - \frac{\partial \eta_{ju}^*}{\partial v} \right), \quad (41)$$

$$\eta_{ju}^{n+1} = \eta_{ju}^* + \frac{\partial \lambda_j^{n+1}}{\partial v} \delta t, \quad \eta_{jv}^{n+1} = \eta_{jv}^* - \frac{\partial \lambda_j^{n+1}}{\partial u} \delta t, \quad (42)$$

$$\delta \theta = \theta(\mathbf{r}_u^*, \mathbf{r}_v^*, \eta_{ju}^{n+1}, \eta_{jv}^{n+1}) - \theta(\mathbf{r}_u^n, \mathbf{r}_v^n, \eta_{ju}^n, \eta_{jv}^n), \quad (43)$$

$$\mathbf{v} = \left( -\frac{\delta \theta}{\theta \delta t}(x - c_1), -\frac{\delta \theta}{\theta \delta t}(y - c_2), v_3^* \right) + \left( -\frac{1}{\theta} \sum_{j=1}^J b_2^{(j)} \frac{\delta \eta_j}{\delta t}, \frac{1}{\theta} \sum_{j=1}^J b_1^{(j)} \frac{\delta \eta_j}{\delta t}, 0 \right), \quad (44)$$

$$\mathbf{r}^{n+1} = \mathbf{r}^n + \mathbf{v} \delta t. \quad (45)$$

Here constanta  $c_1$  and  $c_2$  can be determined by the condition that the projection procedure alone does not lead to extra rigid translation of the grain boundary as discussed above.

Note that in the projected velocity formula in Eq. (44), the first term describes the pure coupling motion of the grain boundary, the second term describes the additional effect of the sliding motion of the grain boundary due to dislocation reaction.

### **Initial dislocation structure**

We assume that the initial grain boundary has an equilibrium dislocation structure that satisfies the Frank's formula and has the lowest energy. See Ref. [34] for the method based on constrained energy minimization to find the equilibrium dislocation structure on a curved low angle grain boundary, which is a generalization of the model for planar low angle grain boundaries [49] examined extensively by comparisons with atomistic simulation results.

## **5 Analysis of the continuum simulation method**

In this section, we summarize some analysis results on the derivation and properties of the continuum model and numerical method.

A simplified form of the local grain boundary energy density in Eq. (6), neglecting the orientation-dependent factor, is  $\tilde{\gamma}_{\text{gb}}(\|\nabla_S \eta_j\|) = -\|\nabla_S \eta_j\| \log \|\nabla_S \eta_j\|$ , which is a concave function of  $\|\nabla_S \eta_j\|$ . In fact,  $\tilde{\gamma}'_{\text{gb}}(\|\nabla_S \eta_j\|) = -\log \|\nabla_S \eta_j\| - 1$  and  $\tilde{\gamma}''_{\text{gb}}(\|\nabla_S \eta_j\|) = -\frac{1}{\|\nabla_S \eta_j\|} < 0$ . We have pointed out in Sec. 2 that such an energy functional will lead to illposed gradient flow. We prove this rigorously in the following theorem.

**Theorem 1** *Consider the energy*

$$E = \int_S f(\|\nabla_S \eta\|) dS, \quad (46)$$

where  $\eta$  is a smooth function defined on the surface  $S$  and  $f$  is a smooth concave function, i.e.,  $f'' < 0$ . The gradient flow due to this energy is

$$\begin{aligned} \frac{\partial \eta}{\partial t} = M_\eta \left[ f''(\|\nabla_S \eta\|) \left( \frac{\nabla_S \eta}{\|\nabla_S \eta\|} \right)^T (\nabla_S \nabla_S \eta) \frac{\nabla_S \eta}{\|\nabla_S \eta\|} \right. \\ \left. + f'(\|\nabla_S \eta\|) \nabla_S \cdot \left( \frac{\nabla_S \eta}{\|\nabla_S \eta\|} \right) \right], \quad (47) \end{aligned}$$

where  $\nabla_S \nabla_S \eta$  is the Hessian of  $\eta$  and mobility  $M_\eta > 0$ . This gradient flow equation is illposed.

*Proof* Consider the energy  $E$  due to  $\eta$  with a small perturbation  $\delta\eta$ . The energy change is

$$\begin{aligned}\delta E &= E[\eta + \delta\eta] - E[\eta] \\ &= \int_S f'(\|\nabla_S \eta\|) \frac{\nabla_S \eta \cdot \nabla_S \delta\eta}{\|\nabla_S \eta\|} dS \\ &= - \int_S \nabla_S \cdot \left( f'(\|\nabla_S \eta\|) \frac{\nabla_S \eta}{\|\nabla_S \eta\|} \right) \delta\eta dS.\end{aligned}\quad (48)$$

Thus

$$\begin{aligned}\frac{\delta E}{\delta\eta} &= - \nabla_S \cdot \left( f'(\|\nabla_S \eta\|) \frac{\nabla_S \eta}{\|\nabla_S \eta\|} \right) \\ &= - \nabla_S f'(\|\nabla_S \eta\|) \cdot \frac{\nabla_S \eta}{\|\nabla_S \eta\|} - f'(\|\nabla_S \eta\|) \nabla_S \cdot \left( \frac{\nabla_S \eta}{\|\nabla_S \eta\|} \right) \\ &= - f''(\|\nabla_S \eta\|) \left( \frac{\nabla_S \eta}{\|\nabla_S \eta\|} \right)^T (\nabla_S \nabla_S \eta) \frac{\nabla_S \eta}{\|\nabla_S \eta\|} \\ &\quad - f'(\|\nabla_S \eta\|) \nabla_S \cdot \left( \frac{\nabla_S \eta}{\|\nabla_S \eta\|} \right).\end{aligned}\quad (49)$$

The gradient flow  $\frac{\partial \eta}{\partial t} = -M_\eta \frac{\delta E}{\delta \eta}$ , where  $M_\eta > 0$ , gives Eq. (47). Recall that  $f''(\|\nabla_S \eta\|) < 0$  in this equation.

We show that the evolution equation (47) is illposed by proof by contradiction.

Assume that the grain boundary  $S$  is expressed by  $\mathbf{r}(u, v)$ , where  $(u, v)$  is an orthogonal parametrization. When  $\eta$  depends only on the parameter  $u$  and  $\eta_u > 0$ , Eq. (47) is reduced to the one-dimensional equation

$$\eta_t = f''(|\eta_u|) \eta_{uu}.\quad (50)$$

Here without loss of generality, we let  $M_\eta = 1$ . Since  $f'' < 0$ , this equation is a backward diffusion equation with variable coefficient.

We consider  $C^2$  solution of the initial value problem with periodic boundary condition in  $u$ , and without loss of generality, let the period be  $2\pi$ . Suppose that Eq. (50) is wellposed for time  $t \in [0, T]$ . There exists a constant  $M > 0$ , such that for any two solutions  $\eta^I$  and  $\eta^{II}$  of Eq. (50) with different initial conditions, we have

$$\|\eta^I(\cdot, t) - \eta^{II}(\cdot, t)\|_{C^2} \leq M \|\eta^I(\cdot, 0) - \eta^{II}(\cdot, 0)\|_{C^2}.\quad (51)$$

Consider two solutions with initial conditions  $\eta^I(u, 0) = pu$  and  $\eta^{II}(u, 0) = pu + \frac{\varepsilon}{k^2} \exp^{iku}$ , where  $p > 0$  is a constant,  $k \geq 1$ , and  $\varepsilon$  is small. We have

$$\|\eta^I(\cdot, 0) - \eta^{II}(\cdot, 0)\|_{C^2} = \varepsilon.\quad (52)$$

We write Eq. (50) as

$$\eta_t = f''(p) \eta_{uu} + g(u, t),\quad (53)$$



where  $g(u, t) = (f''(|\eta_u|) - f''(p))\eta_{uu}$ . Note that  $p + \varepsilon \geq \eta_u^{II}(u, 0) \geq p - \varepsilon$ . We choose  $\varepsilon$  to be small such that  $p - M\varepsilon > 0$ . Using the wellposedness condition in Eq. (51), we have, for  $t \in [0, T]$ ,

$$p + M\varepsilon \geq \eta_u^{II}(u, t) \geq p - M\varepsilon > 0. \quad (54)$$

Consider Fourier transform of these functions, i.e.,  $\eta^{I,II}(u, t) = pu + \sum_k A_k^{I,II}(t) \exp^{iku}$  and  $g(u, t) = \sum_k g_k(t) \exp^{iku}$ . Here  $A_k^I(t) = 0$  for all  $k$ . Using definition of Fourier transform and the wellposedness condition in Eq. (51), we have

$$|A_k^I(t) - A_k^{II}(t)| \leq \|\eta^I(\cdot, t) - \eta^{II}(\cdot, t)\|_{C^0} \leq M\|\eta^I(\cdot, 0) - \eta^{II}(\cdot, 0)\|_{C^2}. \quad (55)$$

Since  $\eta^{II}$  is a solution of Eq. (53), the Fourier coefficient  $A_k^{II}(t)$  of  $\eta^{II}$  satisfies

$$A_k^{II'}(t) = -k^2 f''(p) A_k^{II}(t) + g_k(t). \quad (56)$$

where  $g(u, t) = (f''(|\eta_u^{II}|) - f''(p))\eta_{uu}^{II}$ . Using the initial condition  $A_k^{II}(0) = \frac{\varepsilon}{k^2}$ , the solution of Eq. (56) is

$$A_k^{II}(t) = \frac{\varepsilon}{k^2} e^{-k^2 f''(p)t} + e^{-k^2 f''(p)t} \int_0^t g_k(\tau) e^{k^2 f''(p)\tau} d\tau. \quad (57)$$

Now consider  $g(u, t) = (f''(|\eta_u^{II}|) - f''(p))\eta_{uu}^{II}$ . First,  $f''(|\eta_u^{II}|) - f''(p) = f'''(\xi)(\eta_u^{II} - p)$ , where  $\xi$  is between  $\eta_u^{II}$  and  $p$ . Using the bounds in Eq. (54), we have  $|\eta_u^{II} - p| \leq M\varepsilon$ , and  $|f'''(\xi)| \leq C_p$ , where  $C_p$  is a constant depending on  $p$ . Moreover, since  $\eta_{uu}^{II} = \eta_{uu}^{II} - \eta_{uu}^I$ , we have  $|\eta_{uu}^{II}| = |\eta_{uu}^{II} - \eta_{uu}^I| \leq M\|\eta^I(\cdot, 0) - \eta^{II}(\cdot, 0)\|_{C^2} = M\varepsilon$ . Using these results, we have

$$|g_k(t)| \leq \max_u |g(u, t)| \leq C_p M^2 \varepsilon^2. \quad (58)$$

Thus, the integral in second term in  $A_k^{II}(t)$  in Eq. (57) can be bounded as  $|\int_0^t g_k(\tau) e^{k^2 f''(p)\tau} d\tau| \leq \int_0^t \varepsilon^2 C_p M^2 e^{k^2 f''(p)\tau} d\tau = \frac{\varepsilon^2 C_p M^2}{k^2 f''(p)} (e^{k^2 f''(p)t} - 1)$ . Therefore, we have

$$|A_k^I(t) - A_k^{II}(t)| = |A_k^{II}(t)| \geq \frac{\varepsilon}{k^2} e^{-k^2 f''(p)t} \left[ 1 - \frac{C_p M^2}{-f''(p)} \varepsilon (1 - e^{k^2 f''(p)t}) \right]. \quad (59)$$

We choose  $\varepsilon$  to be small enough such that  $1 - \frac{C_p M^2}{-f''(p)} \varepsilon > 0$ .

Since  $f''(p) < 0$ , Eqs. (59) and (52) contradict with Eq. (55) as  $k \rightarrow \infty$ .

*Remark 1* With the actual local energy density in Eq. (6), we have  $\frac{\delta E_{\text{local}}}{\delta \eta_j} = \mathbf{f}_{\text{local}}^{(j)} \cdot \frac{\nabla_s \eta_j}{\|\nabla_s \eta_j\|}$ , where  $\mathbf{f}_{\text{local}}^{(j)}$  is given by Eq. (9). Illposedness of the gradient flow  $\frac{\partial \eta_j}{\partial t} = -M_\eta \frac{\delta E}{\delta \eta_j}$  associated with this energy formula can be proved similarly.

*Remark 2* Illposedness of the gradient flow comes from the Hessian term in Eq. (47), or in Eq. (9) for the actual evolution equation. In the previous models [51, 52], this term was removed when the driving force is dominated by the long-range force (Eqs. (7) and (8)). However, in the grain boundary dynamics problem, the long-range force is essentially canceled during the evolution, and this Hessian term due the local energy plays critical roles and cannot be removed from the equation.

Next, in the following theorem, we show existence and uniqueness of the projection operation used in Sec. 3. This theorem plays the same role as the Helmholtz–Hodge decomposition theorem in the projection method for solving fluid dynamics problems [9].

**Theorem 2** *Given a smooth vector function  $\zeta = (\zeta_1, \zeta_2)$  in a periodic  $(u, v)$  domain, there exist a unique periodic vector function  $\zeta^{\tilde{D}} = (\zeta_1^{\tilde{D}}, \zeta_2^{\tilde{D}})$  and a periodic function  $\lambda$  such that*

$$\zeta = \zeta^{\tilde{D}} + \tilde{\mathbf{G}}\lambda, \quad (60)$$

where

$$\tilde{D}\zeta^{\tilde{D}} = \frac{\partial \zeta_1^{\tilde{D}}}{\partial v} - \frac{\partial \zeta_2^{\tilde{D}}}{\partial u} = 0, \quad (61)$$

and

$$\tilde{\mathbf{G}}\lambda = \left( \frac{\partial \lambda}{\partial v}, -\frac{\partial \lambda}{\partial u} \right). \quad (62)$$

*Proof* We first prove existence of  $\zeta^{\tilde{D}}$ . If  $\zeta = \zeta^{\tilde{D}} + \tilde{\mathbf{G}}\lambda$  holds, we have  $\tilde{D}\zeta = \Delta\lambda$ , where  $\Delta$  is the Laplacian operator. Under periodic boundary condition, the solution  $\lambda$  is unique up to addition of a constant. With the solved  $\lambda$ , we can define  $\zeta^{\tilde{D}} = \zeta - \tilde{\mathbf{G}}\lambda$ .

Now we proof uniqueness of  $\zeta^{\tilde{D}}$ . If  $\zeta^{\tilde{D}}$  exists, we have

$$\langle \zeta^{\tilde{D}}, \tilde{\mathbf{G}}\lambda \rangle = - \langle \tilde{D}\zeta^{\tilde{D}}, \lambda \rangle = 0,$$

where the inner product  $\langle f, g \rangle = \int_D fg \, dudv$  with  $D$  being the periodic domain. This gives  $\|\zeta\|^2 = \|\zeta^{\tilde{D}}\|^2 + \|\tilde{\mathbf{G}}\lambda\|^2$ , where  $\|\cdot\|$  is the  $L_2$ -norm over  $D$ . Thus, we have  $\zeta^{\tilde{D}} = \mathbf{0}$  when  $\zeta = \mathbf{0}$ , from which uniqueness of  $\zeta^{\tilde{D}}$  follows.

*Remark 3* From the proof of Theorem 2, we have  $\|\zeta\|^2 = \|\zeta^{\tilde{D}}\|^2 + \|\tilde{\mathbf{G}}\lambda\|^2$  and  $\langle \zeta^{\tilde{D}}, \tilde{\mathbf{G}}\lambda \rangle = 0$ . These mean that  $\zeta^{\tilde{D}}$  is the projection of  $\zeta$  that satisfies Eq. (61).

*Remark 4* In the second step in the projection method used in Sec. 3, i.e., Eq. (22), we project the result  $(\eta_{ju}^*, \eta_{jv}^*)$  in Eqs. (20) and (21) obtained in the first step without constraint, to the result  $(\eta_{ju}^{n+1}, \eta_{jv}^{n+1})$  that satisfies the constraint  $\tilde{D}(\eta_{ju}^{n+1}, \eta_{jv}^{n+1}) = \frac{\eta_{ju}^{n+1}}{\partial v} - \frac{\eta_{jv}^{n+1}}{\partial u} = 0$ , and  $-\lambda_j^{n+1}\delta t$  in Eq. (22) is the function  $\lambda$  in Theorem 2.

## 6 Numerical simulations

In this section, we perform numerical simulations of grain boundary dynamics using our numerical algorithm in Eqs. (38)-(45), which is a numerical implementation of the continuum model of constrained evolution in Eqs. (24)–(27). The numerical simulation results are compared extensively with those obtained by atomistic-level simulations using phase field crystal model [45] and amplitude expansion phase field crystal model [36] for various properties of coupling and sliding motions of the grain boundary to validate our continuum model. Convergence tests show that the proposed continuum simulation algorithm indeed fixes the problem of illposedness and that the projection algorithms converge.

We consider grain boundaries in fcc Al. We choose the directions  $[\bar{1}10]$ ,  $[\bar{1}\bar{1}2]$ ,  $[111]$  to be the  $x$ ,  $y$  and  $z$  directions, respectively. In this coordinate system, the six Burgers vectors are  $\mathbf{b}^{(1)} = (1, 0, 0)b$ ,  $\mathbf{b}^{(2)} = \left(\frac{1}{2}, \frac{\sqrt{3}}{2}, 0\right)b$ ,  $\mathbf{b}^{(3)} = \left(\frac{1}{2}, -\frac{\sqrt{3}}{2}, 0\right)b$ ,  $\mathbf{b}^{(4)} = \left(0, \frac{\sqrt{3}}{3}, -\frac{\sqrt{6}}{3}\right)b$ ,  $\mathbf{b}^{(5)} = \left(\frac{1}{2}, \frac{\sqrt{3}}{6}, \frac{\sqrt{6}}{3}\right)b$ , and  $\mathbf{b}^{(6)} = \left(-\frac{1}{2}, \frac{\sqrt{3}}{6}, \frac{\sqrt{6}}{3}\right)b$ , where  $b$  is the magnitude of the Burgers vectors. In Al,  $b = 0.286\text{nm}$  and the Poisson ratio is  $\nu = 0.347$ . The rotation axis  $\mathbf{a}$  is in the  $[111]$  direction, i.e.,  $+z$  direction.

We study the evolution of an initially spherical grain boundary, whose radius is  $R = 20b$  and misorientation angle is  $\theta = 5^\circ$ . There are three sets of dislocations with Burgers vectors  $\mathbf{b}^{(1)}$ ,  $\mathbf{b}^{(2)}$ , and  $\mathbf{b}^{(3)}$ , respectively, in the equilibrium dislocation structure on this initial, spherical grain boundary; see the top image in Fig. 3(a).

In the dynamics simulation, the grain boundary is parameterized using spherical coordinates  $R = R(\alpha, \beta)$ , for  $0 \leq \alpha < 2\pi$  and  $0 \leq \beta \leq \pi$ . Here  $\alpha$  is the angle between the position vector of a point on the grain boundary and the  $x$  axis, and  $\beta$  is the angle between the position vector of the point and the  $z$  axis. Initially,  $R(\alpha, \beta) = 20b$ . The  $(\alpha, \beta)$  domain is discretized into  $40 \times 20$  uniform grids during the evolution. The center of the spherical grain boundary is the origin  $(0, 0, 0)$  in the coordinate system. Due to symmetry, the two constants  $c_1 = c_2 = 0$  in the projected velocity formula in Eq. (44). Simulation of one example took less than two minutes on a laptop with a single i7-6500u processor.

### 6.1 Convergence of the numerical algorithm

We perform convergence tests in time for our numerical algorithm to show that the problem of illposedness has been fixed and the projection algorithms converge.

We examine the misorientation angle  $\theta$  and the surface area  $S_A$  of the grain boundary during the evolution up to time  $t = 20.8/M_d\mu$  with different values of time step  $\delta t$ . Recall that the misorientation angle  $\theta$  is calculated

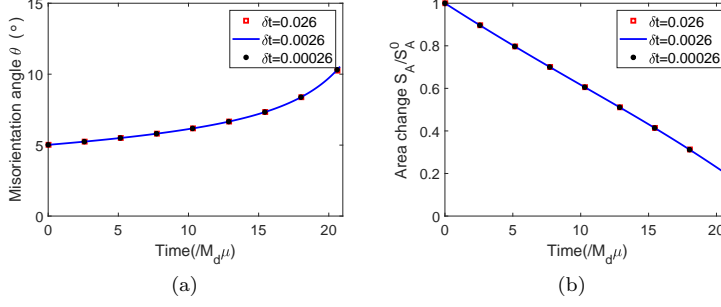


**Fig. 2** Evolutions of (a) misorientation angle  $\theta$  and (b) surface area  $S_A$  of the grain boundary during the evolution with different values of time step  $\delta t$ .

using Eq. (30) and surface area  $S_A = \int_S \|\mathbf{r}_u \times \mathbf{r}_v\| du dv$ . The surface area of the initial grain boundary is denoted as  $S_A^0$ . Evolutions of these two quantities are shown in Fig. 2, from which convergence can be seen with different values of time step  $\delta t$ .

**Table 1** Misorientation angle  $\theta$  and surface area  $S_A$  at time  $t = 20.8/M_d\mu$ .

$\delta t/(M_d\mu)$	Misorientation Angle $\theta(^{\circ})$	$Q_{\theta}$	Surface Area ( $S_A/S_A^0$ )	$Q_{S_A}$
0.416000	9.18428427	1.6214	0.25978820	1.7900
0.208000	9.78932770	2.0195	0.22902276	2.0263
0.104000	10.16249512	1.9196	0.21183550	1.9543
0.052000	10.34727401	1.9422	0.20335333	1.9691
0.026000	10.44353091	1.9794	0.19901303	1.9929
0.013000	10.49309176		0.19680884	
0.006500	10.51813002		0.19570282	

We further examine the orders of convergence of  $\theta$  and  $S_A$ , and the results are shown in Table 1. The ratio  $Q_g = \frac{g_{\delta t} - g_{\frac{\delta t}{2}}}{g_{\frac{\delta t}{2}} - g_{\frac{\delta t}{4}}}$ , where  $g_{\delta t}$  is the numerical value of  $g$  at time  $\delta t$ . These results show a first order convergence of the numerical algorithm. These validate our numerical algorithm, and especially, there is no numerical instability and the projection algorithms that we employ converge.

## 6.2 Pure coupling motion

We first consider the grain boundary motion without dislocation reaction, i.e. the reaction mobility  $M_r = 0$  in Eq. (40), and accordingly  $\delta\eta_j = 0$  in Eq. (44). This is the pure coupling motion.

Fig. 3 shows the shrinkage of the spherical grain boundary under this pure coupling motion. The grain boundary eventually disappears. In this case, since  $M_r = 0$  and  $\delta\eta_j = 0$ , the grain boundary velocity in Eq. (44) becomes  $\mathbf{v} =$

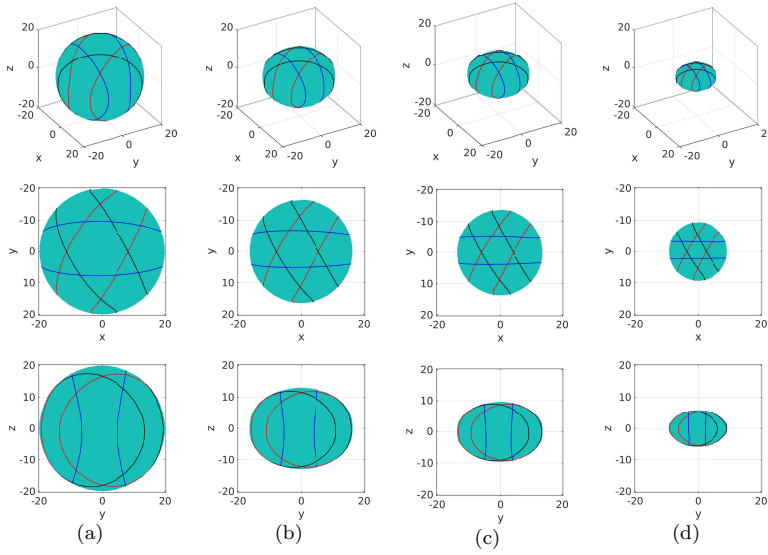


**Fig. 3** Shrinkage of an initially spherical grain boundary in fcc under pure coupling motion, i.e., without dislocation reaction. The rotation axis is the  $z$  direction ( $[111]$ ), and the initial misorientation angle  $\theta = 5^\circ$ . The upper panel of images show the three-dimensional view of the grain boundary during evolution. The middle panel of images show the grain boundary during evolution viewed from the  $+z$  direction ( $[111]$ ), and the lower panel of images show the grain boundary during evolution viewed from the  $+x$  direction ( $[\bar{1}10]$ ). Dislocations with Burgers vectors  $\mathbf{b}^{(1)}$ ,  $\mathbf{b}^{(2)}$  and  $\mathbf{b}^{(3)}$  are shown by blue, black and red lines, respectively. Length unit:  $b$ . (a) The initial spherical grain boundary. (b), (c), and (d) Configurations at time  $t = 10/M_d\mu$ ,  $15/M_d\mu$ ,  $20/M_d\mu$ , respectively.

$-\frac{\delta\theta}{\delta t}(x, y, 0) + (0, 0, v_3^*)$ . In the direction normal the rotation axis, i.e., in the  $xy$  plane, the velocity component is in the inward radial direction, as in the two-dimensional model [50, 48]; this is adjusted from the velocity component due to curvature flow in order to satisfy the Frank's formula. Whereas in the direction of the rotation axis, i.e., the  $z$  direction, there is no constraint imposed by the Frank's formula, and the velocity component is the same as that in the curvature flow.

As an example, we consider the cross-section of the grain boundary with the  $z = 0$  plane (i.e., cross-section normal to the  $[111]$  rotation axis), which is the equator of the grain boundary in the three dimensional view in the upper panel in Fig. 3 and is a circle (the outer circle) as shown in the second panel in Fig. 3 for the view from  $+z$  direction. The grain boundary along this circular cross-section is pure tilt, which is similar to the two-dimensional grain boundary discussed in Ref. [50, 48]. Along this circle, during the evolution, we have  $\mathbf{v}_3^* = 0$ , and the grain boundary velocity is  $\mathbf{v} = -\frac{\delta\theta}{\delta t}(x, y, 0)$ , which is completely in the inward radial direction in the  $z = 0$  plane. Thus the cross-section keeps the circular shape as it shrinks during the evolution, as shown in the second

panel in Fig. 3. This shape-preserving evolution agrees with the results of the two-dimensional grain boundary dynamics models [40,50,48] and shrinkage of circular grain boundaries in two dimensions by molecular dynamics [38] and phase field crystal [44] simulations. However, here the changing rate of misorientation angle  $\frac{\delta\theta}{\delta t}$  in the velocity formula is depending on the entire grain boundary in three dimensions by Eq. (43), and is not just depending on the circular cross-section itself as in the two dimensional continuum model [48].

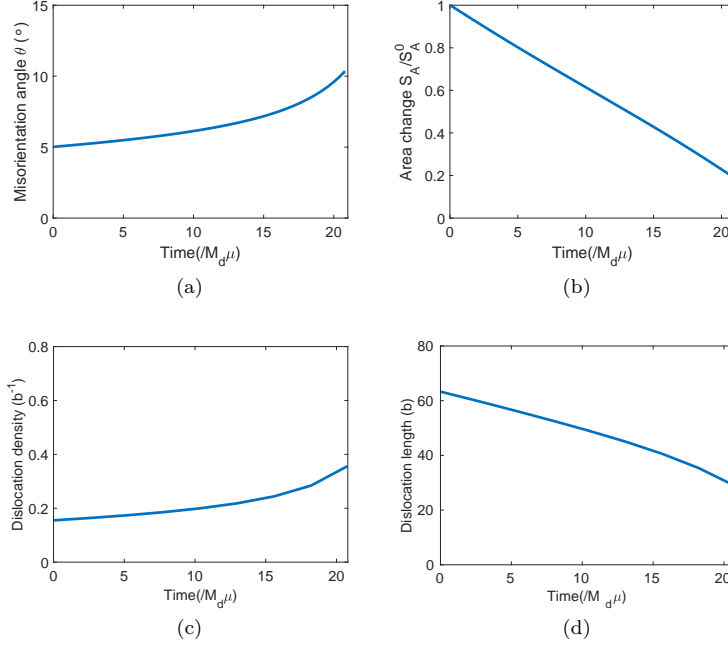
Next, we consider the cross-section of the grain boundary with the  $x = 0$  plane (i.e., cross-section normal to the  $[\bar{1}10]$  direction); see the lower panel in Fig. 3 (the outer boundary of the projected grain boundary surface). Initially, the cross-section is a circle, and it gradually changes to an ellipse as it shrinks during the evolution. This shows that the velocity in the rotation axis direction, i.e.  $z$  direction is larger than that in the  $x$  and  $y$  directions. The reason for this anisotropic motion is that there is no constraint of Frank's formula in the  $z$  direction which is the direction of the rotation axis, and the velocity at the two poles on the grain boundary with respect to the  $z$  direction (where the grain boundary is pure twist) is the same as that in the curvature flow; whereas the velocity components in the  $x$  and  $y$  directions are adjusted from those in the curvature flow by the constraint of the Frank's formula, and the resulting velocity in the  $xy$  plane are depending on the entire grain boundary through the coefficient  $\delta\theta$ , as discussed above. Evolution of this initially spherical grain boundary and its dislocation structure, especially the property that the shrinkage of the grain boundary is faster in the direction of the rotation axis than in other directions, agree with the results of atomistic-level simulations using phase field crystal model [45] and amplitude expansion phase field crystal model [36].

Fig. 4(a) shows the change of misorientation angle  $\theta$  during the evolution, which is continuously increasing. This behavior agrees with Cahn-Taylor theory [6], three dimensional phase-field crystal simulations [45], and two-dimensional atomistic [38,41], phase field crystal [44], and continuum [50,48] simulations. Such increasing of misorientation angle cannot be obtained by the classical motion by mean curvature models or pure sliding models, in which the misorientation angle is constant or is decreasing during the evolution.

Fig. 4(b) shows evolution of the area of the grain boundary, which reveals the relation:

$$\frac{S_A(t)}{S_A^0} = 1 - At, \quad (63)$$

where  $A$  is some constant, and  $S_A(t)$  and  $S_A^0$  are the grain boundary area at time  $t$  and that of the initial configuration, respectively. This agrees with the results of nearly linear decrease of the grain boundary area using amplitude expansion phase field crystal model for grain boundaries in both fcc and bcc crystals [36]. The phase field crystal simulations in Ref. [45] showed that the decrease of the volume of the grain enclosed by an initially spherical low angle grain boundary in a bcc crystal approximately follows the relation  $\frac{V^{2/3}(t)}{V_0^{2/3}} =$



**Fig. 4** Shrinkage of an initially spherical grain boundary in fcc under pure coupling motion. The rotation axis is the  $z$  direction ( $[111]$ ), and the initial misorientation angle  $\theta = 5^\circ$ . (a) Evolution of misorientation angle  $\theta$ . (b) Evolution of grain boundary area  $S_A$ , where  $S_A^0$  is the area of the initial grain boundary. (c) Evolution of density of dislocations with Burgers vector  $\mathbf{b}^{(1)}/\mathbf{b}^{(2)}/\mathbf{b}^{(3)}$  on the grain boundary. (d) Evolution of the total length of dislocations with Burgers vector  $\mathbf{b}^{(1)}/\mathbf{b}^{(2)}/\mathbf{b}^{(3)}$  on the grain boundary. In (c) and (d), the densities and total lengths of dislocations with these three Burgers vectors are almost identical.

$1 - A_1 t$ , where  $A_1$  is some constant, and  $V(t)$  and  $V_0$  are the volume of the grain enclosed by the grain boundary at time  $t$  and that of the initial configuration, respectively. It was argued in Ref. [45] that their results are consistent with the result of classical Von Neumann-Mullins relation [33] for a two dimensional grain boundary driven by curvature with constant energy density, i.e., Eq. (63) if  $S_A$  denotes the area enclosed by the grain boundary in two dimensions, considering the approximate relation  $V^{2/3} \sim S_A$ . In this sense, simulation results using our continuum model and the amplitude expansion phase field crystal simulations in [36] are consistent with the results in Ref. [45] as well as the result of the classical Von Neumann-Mullins relation. The nearly linear decrease of the grain boundary area in Eq. (63) obtained by our continuum model and the amplitude expansion phase field crystal model in Ref. [36] is also in consistent with the result that the area enclosed by a two dimensional grain boundary is linearly decreasing in the two dimensional phase field crystal

simulations for circular grain boundaries [44] and continuum model simulations for circular [50] and general shape [48] grain boundaries in two dimensions.

Evolutions of dislocation densities on the grain boundary and total length of dislocations are shown in Figs. 4(c) and (d). It can be seen from Fig. 4(c) that the densities of the dislocations with all the three Burgers vectors are increasing during the evolution. This is consistent with the increase of misorientation angle  $\theta$  during the evolution. The total length of dislocations is decreasing during the evolution as shown in Fig. 4(d). This is in agreement with the phase field crystal simulation results in Ref. [45]. Unlike in the two dimensional case with dislocation conservation [38, 6, 41, 44, 50, 48] where dislocations are infinite straight lines, in three dimensions without dislocation reaction, the constituent dislocations are closed loops, and all the dislocation loops are shrinking and the total length of dislocations is decreasing as the grain boundary shrinks.

### 6.3 Motion with dislocation reaction

Now we perform simulations using our continuum model considering dislocation reaction, i.e.  $M_r \neq 0$ . Dislocation reaction leads to removal of dislocations, resulting in the coupling motion of the grain boundary [38, 6, 41, 45, 50, 48]. The mobility  $M_r$  is a temperature-dependent material parameter, and it may also depend on the local dislocation reaction mechanism [41, 45]. We set  $M_r$  to be constant in our simulations to examine the effect of dislocation reaction. We use the same initial spherical grain boundary as in Sec. 6.2 without dislocation reaction.

Fig. 5 shows the shrinkage of the initially spherical grain boundary with dislocation reaction, where the reaction mobility  $M_r b^3 / M_d = 1.83 \times 10^{-4}$ . We consider the cross-section of the grain boundary with the  $z = 0$  plane (i.e., cross-section normal to the [111] rotation axis), which is the equator of the grain boundary in the three dimensional view in the upper panel in Fig. 5 and the outer curve in the view from the  $+z$  axis in the second panel in Fig. 5. Along this curve, the grain boundary is pure tilt everywhere, and we have  $v_3^* = 0$ , i.e., the velocity is always in the  $z = 0$  plane during the evolution. The evolution of this curve is similar to that of the two-dimensional grain boundary discussed in [50, 48]. The initial circular cross-section gradually changes to a hexagonal shape as it shrinks. Each edge in this hexagon is pure tilt that consists of dislocations of only one Burgers vector. This behavior is consistent with the fact that the energy density of the grain boundary is anisotropic and the pure tilt boundary has the minimum energy of all tilt boundaries, and is the same as the evolution of two dimensional grain boundary with dislocation reaction obtained in [50, 48].

The lower panel of Fig. 5 shows the evolution of the grain boundary in the view from the  $+x$  direction ( $[\bar{1}10]$  direction). The cross-section of the grain boundary with the  $x = 0$  plane gradually changes to an ellipse as it shrinks. These behaviors of the evolution of the initially spherical grain boundary with



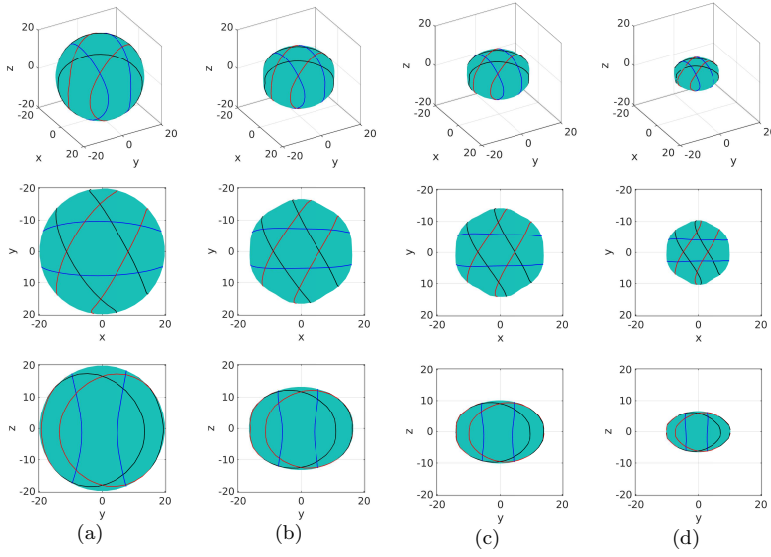


**Fig. 5** Shrinkage of an initially spherical grain boundary in fcc with dislocation reaction:  $M_r b^3 / M_d = 1.83 \times 10^{-4}$ . The rotation axis is the  $z$  direction ( $[111]$ ), and the initial misorientation angle  $\theta = 5^\circ$ . The upper panel of images show the three-dimensional view of the grain boundary during evolution. The middle panel of images show the grain boundary during evolution viewed from the  $+z$  direction ( $[111]$ ), and the lower panel of images show the grain boundary during evolution viewed from the  $+x$  direction ( $[\bar{1}10]$ ). Dislocations with Burgers vectors  $\mathbf{b}^{(1)}$ ,  $\mathbf{b}^{(2)}$  and  $\mathbf{b}^{(3)}$  are shown by blue, black and red lines, respectively. Length unit:  $b$ . (a) The initial spherical grain boundary. (b), (c), and (d) Configurations at time  $t = 10/M_d \mu$ ,  $15/M_d \mu$ ,  $20/M_d \mu$ , respectively.

dislocation reaction in an fcc crystals are similar to the phase field crystal simulation results of an initially spherical grain boundary in a bcc crystal [45].

Evolution of the misorientation angle  $\theta$  with different values of reaction mobility  $M_r$  is shown in Fig. 6(a). When  $M_r \neq 0$ , the evolution of misorientation angle is controlled by both the coupling effect and sliding effect. As can be seen from Fig. 6(a), the misorientation angle  $\theta$  is increasing during the evolution except for the case with very high dislocation reaction mobility; as the dislocation reaction mobility  $M_r$  increases, meaning the sliding effect due to dislocation reaction is becoming stronger, the increase rate of  $\theta$  decreases, and when the sliding effect is strong enough, the misorientation angle  $\theta$  is decreasing. These properties are the same as those in the two-dimensional cases [50, 48]: the coupling motion of grain boundary associated with the conservation of dislocations will increase the misorientation angle  $\theta$  during the evolution, and the sliding motion generated by dislocation reaction will decrease  $\theta$ . These results also suggest a way to tune the parameter  $M_r$  based on the evolution of misorientation angle measured by experiments or atomistic simulations.

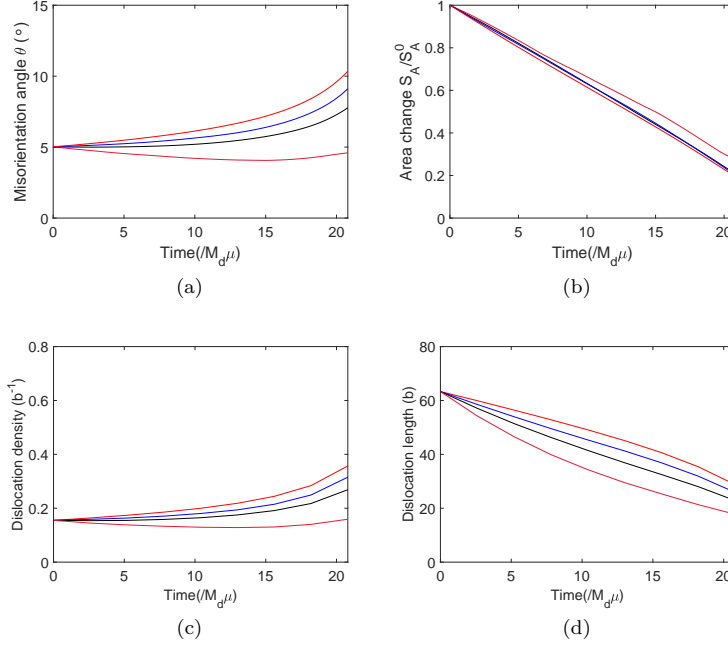


**Fig. 6** Shrinkage of an initially spherical grain boundary in fcc with different values of reaction mobility  $M_r$ . The rotation axis is the  $z$  direction ([111]), and the initial misorientation angle  $\theta = 5^\circ$ . The reaction mobility  $M_r b^3 / M_d = 0, 9.16 \times 10^{-5}, 1.83 \times 10^{-4},$  and  $3.74 \times 10^{-4}$  from the top curve to the bottom one in (a), (c) and (d), and from the bottom to the top ones in (b). (a) Evolution of misorientation angle  $\theta$ . (b) Evolution of grain boundary area  $S_A$ , where  $S_A^0$  is the area of the initial grain boundary. (c) Evolution of density of dislocations with Burgers vector  $\mathbf{b}^{(1)}/\mathbf{b}^{(2)}/\mathbf{b}^{(3)}$  on the grain boundary. (d) Evolution of the total length of dislocations with Burgers vector  $\mathbf{b}^{(1)}/\mathbf{b}^{(2)}/\mathbf{b}^{(3)}$  on the grain boundary. In (c) and (d), the densities and total lengths of dislocations with these three Burgers vectors are almost identical.

Fig. 6(b) shows the evolution of grain boundary area with different values of dislocation reaction mobility  $M_r$ . It can be seen that except for the case with very high dislocation reaction mobility, the decrease of grain boundary area still follows the linear law in Eq. (63), and is almost unchanged with different values of dislocation reaction mobility. In the case with very high dislocation reaction mobility  $M_r = 3.74 \times 10^{-4} M_d / b^3$ , the decrease of grain boundary area starts to deviate from the linear law with slower decreasing rate, which is due to the resulting significant decrease in the grain boundary energy density that slows down the shrinking of the grain boundary. Again, the linear decrease of grain boundary area is consistent with the available phase field crystal and amplitude expansion phase field crystal simulation results [45,36].

Evolutions of dislocation densities on the grain boundary and total length of dislocations with different values of reaction mobility  $M_r$  are shown in

Figs. 6(c) and (d). As can be seen from Fig. 6(c), the densities of the dislocations with all the three Burgers vectors are increasing during the evolution except for the case with very high dislocation reaction mobility; as the dislocation reaction mobility  $M_r$  increases, the increase rate of dislocation densities decreases, and when the dislocation reaction mobility is high enough, the dislocation densities are decreasing. These behaviors are consistent with the increase of misorientation angle  $\theta$  during the evolution shown in Fig. 6(a). Fig. 6(d) shows that the total length of dislocations is decreasing as the grain boundary shrinks, and the decrease rate is higher for higher dislocation reaction mobility  $M_r$ . The decrease of the total length of dislocations is in agreement with the phase field crystal simulation results in Ref. [45].

## 7 Conclusions

We have developed a continuum model for the dynamics of grain boundaries in three dimensions that incorporates the motion and reaction of the constituent dislocations. The continuum model includes evolution equations for both the motion of the grain boundary and the evolution of dislocation structure on the grain boundary. The evolution of orientation-dependent continuous distributions of dislocation lines on the grain boundary is based on the simple representation using dislocation density potential functions. This simple representation method also guarantees continuity of the dislocation lines on the grain boundaries during the evolution.

In order to overcome the illposedness in formulation that comes from the nonconvexity of the energy density, we use the components of the surface gradients of the dislocation density potential functions instead of these functions directly. Relationship between the components of these surface gradients (i.e. continuity of dislocation lines) is maintained by the projection method during the evolution. The critical but computationally expensive long-range elastic interaction of dislocations is replaced by a projection formulation that maintains the constraint of the Frank's formula describing the equilibrium of the strong long-range interaction. This continuum model is able to describe the grain boundary motion and grain rotation due to both coupling and sliding effects, to which the classical motion by mean curvature model does not apply.

Using the obtained continuum model, simulations are performed for the dynamics of initially spherical low angle grain boundaries in fcc Al, under the conditions without dislocation reaction (pure coupling motion) and with dislocation reaction (with sliding motion). The simulations have shown increase of the misorientation angle as the grain boundary shrinks under the effect of conservation of dislocations, anisotropic motion in the directions along and normal the rotation axis, anisotropic motion in the normal plane with respect to the rotation axis due to dislocation reaction, and linear decrease of grain boundary area. These results agree well with those of atomistic simulations (phase field crystal and amplitude expansion phase field crystal simulations) [45,36]. The simulation results are also consistent with previously obtained

results using continuum model in two dimensions [50,48]. In particular, we explain the anisotropic motion in the directions along and normal the rotation axis by the fact that the constraint of Frank's formula only has effect in a direction normal to the rotation axis, and the motion is free in the direction of the rotation axis.

The continuum model presented in this paper provides a basis for continuum simulations of evolution of grain boundary networks at larger length scales [25,30,27]. This will be explored in the future work. This continuum simulation framework for the distribution and dynamics of curves on curved surfaces can also be applied more generally beyond the dynamics of dislocations and grain boundaries.

### Acknowledgement

This work was supported by the Hong Kong Research Grants Council General Research Fund 16301720 and 16302818.

### Data availability

The datasets generated in study are available upon reasonable request.

### A Derivation of the formula for misorientation angle $\theta$ in (30)

Substituting  $\mathbf{V}_1 = \mathbf{r}_u$  and  $\mathbf{V}_2 = \mathbf{r}_v$  into Frank's formula in Eq. (27), we have

$$\theta(\mathbf{r}_u \times \mathbf{a}) - \sum_{j=1}^J \mathbf{b}^{(j)} \eta_{ju} = 0, \quad (64)$$

$$\theta(\mathbf{r}_v \times \mathbf{a}) - \sum_{j=1}^J \mathbf{b}^{(j)} \eta_{jv} = 0. \quad (65)$$

Here we have used  $\nabla_S \eta_j \cdot \mathbf{r}_u = \eta_{ju}$  and  $\nabla_S \eta_j \cdot \mathbf{r}_v = \eta_{jv}$ . Adding the two equations (64) and (65), multiplying both size of the summation by  $(\mathbf{r}_u + \mathbf{r}_v) \times \mathbf{a}$ , we have

$$\theta \|(\mathbf{r}_u + \mathbf{r}_v) \times \mathbf{a}\|^2 = \sum_{j=1}^J (\eta_{ju} + \eta_{jv}) (\mathbf{r}_u + \mathbf{r}_v) \times \mathbf{a} \cdot \mathbf{b}^{(j)}. \quad (66)$$

Integrating over the entire grain boundary  $S$ , we obtain the formula of  $\theta$  in Eq. (30).

### References

1. Admal, N.C., Po, G., Marian, J.: A unified framework for polycrystal plasticity with grain boundary evolution. *Int. J. Plasticity* **106**, 1–30 (2018)
2. Ask, A., Forest, S., Appolaire, B., Ammar, K., Salman, O.U.: A cosserat crystal plasticity and phase field theory for grain boundary migration. *J. Mech. Phys. Solids* **115**, 167–194 (2018)

3. Basak, A., Gupta, A.: A two-dimensional study of coupled grain boundary motion using the level set method. *Modell. Simul. Mater. Sci. Eng.* **22**, 055022 (2014)
4. Bilby, B.A.: Bristol conference report on defects in crystalline materials. *Phys. Soc.*, London p. 123 (1955)
5. Cahn, J.W., Mishin, Y., Suzuki, A.: Coupling grain boundary motion to shear deformation. *Acta Mater.* **54**, 4953–4975 (2006)
6. Cahn, J.W., Taylor, J.E.: A unified approach to motion of grain boundaries, relative tangential translation along grain boundaries, and grain rotation. *Acta Mater.* **52**, 4887–4898 (2004)
7. Chen, L.Q., Yang, W.: Computer simulation of the domain dynamics of a quenched system with a large number of nonconserved order parameters: The grain-growth kinetics. *Phys. Rev. B* **50**, 15752–15756 (1994)
8. Chorin, A.J.: Numerical solution of the navier-stokes equations. *Math. Comp.* **22**, 745–762 (1968)
9. Chorin, A.J., Marsden, J.E., Marsden, J.E.: A mathematical introduction to fluid mechanics, vol. 168. Springer (1990)
10. Coddington, E.A., Levinson, N.: *Theory of Ordinary Differential Equations*. McGraw-Hill, New York (1955)
11. Dai, S., Li, B., Lu, J.: Convergence of phase-field free energy and boundary force for molecular solvation. *Arch. Ration. Mech. Anal.* **227**, 105–147 (2018)
12. Du, Q., Feng, X.B.: The phase field method for geometric moving interfaces and their numerical approximations. *Handbook of Numerical Analysis* **21**, 425–508 (2020)
13. Elsey, M., Esedoglu, S., Smereka, P.: Diffusion generated motion for grain growth in two and three dimensions. *J. Comput. Phys.* **228**, 8015–8033 (2009)
14. Epshteyn, Y., Liu, C., Mizuno, M.: Motion of grain boundaries with dynamic lattice misorientations and with triple junctions drag. *SIAM J. Math. Anal.* **53**, 3072–3097 (2021)
15. Esedoglu, S.: Grain size distribution under simultaneous grain boundary migration and grain rotation in two dimensions. *Comput. Mater. Sci.* **121**, 209–216 (2016)
16. Feng, X., Prohl, A.: Numerical analysis of the Allen-Cahn equation and approximation for mean curvature flows. *Numer. Math.* **94**, 33–65 (2003)
17. Frank, F.C.: *The resultant content of dislocations in an arbitrary intercrystalline boundary*. pp. 150–154. Office of Naval Research, Pittsburgh (1950)
18. Gorkaya, T., Molodov, D.A., Gottstein, G.: Stress-driven migration of symmetrical  $< 100 >$  tilt grain boundaries in al bicrystals. *Acta Mater.* **57**, 5396–5405 (2009)
19. Harris, K., Singh, V., King, A.: Grain rotation in thin films of gold. *Acta Mater.* **46**, 2623–2633 (1998)
20. Herring, C.: Surface tension as a motivation for sintering. In: W.E. Kingston (ed.) *The Physics of Powder Metallurgy*, pp. 143–179. McGraw-Hill, New York (1951)
21. Kazaryan, A., Wang, Y., Dregia, S.A., Patton, B.R.: Generalized phase-field model for computer simulation of grain growth in anisotropic systems. *Phys. Rev. B* **61**, 14275–14278 (2000)
22. Kinderlehrer, D., Liu, C.: Evolution of grain boundaries. *Math. Models Methods Appl. Sci.* **4**, 713–729 (2001)
23. Kirch, D.M., Jannot, E., Barrales-Mora, L.A., Molodov, D.A., Gottstein, G.: Inclination dependence of grain boundary energy and its impact on the faceting and kinetics of tilt grain boundaries in aluminum. *Acta Mater.* **56**, 4998–5011 (2006)
24. Kobayashi, R., Warren, J.A., Carter, W.C.: A continuum model of grain boundaries. *Phys. D* **140**, 141–150 (2000)
25. Krill III, C., Chen, L.Q.: Computer simulation of 3-d grain growth using a phase-field model. *Acta Mater.* **50**, 3059–3075 (2002)
26. Lazar, E.A., MacPherson, R.D., Srolovitz, D.J.: A more accurate two-dimensional grain growth algorithm. *Acta Mater.* **58**, 364–372 (2010)
27. Le, T., Du, Q.: A generalization of the three-dimensional macpherson-srolovitz formula. *Commun. Math. Sci.* **7**, 511–520 (2009)
28. Li, C.H., Edwards, E.H., Washburn, J., Parker, E.R.: Stress-induced movement of crystal boundaries. *Acta Metall.* **1**, 223–229 (1953)
29. Li, J.C.: Possibility of subgrain rotation during recrystallization. *J. Appl. Phys.* **33**, 2958–2965 (1962)

30. MacPherson, R., Srolovitz, D.: The von neumann relation generalized to coarsening of three-dimensional microstructures. *Nature* **446**, 1053–105 (2007)
31. McReynolds, K., Wu, K.A., Voorhees, P.: Grain growth and grain translation in crystals. *Acta Mater.* **120**, 264–272 (2016)
32. Molodov, D.A., Ivanov, V.A., Gottstein, G.: Low angle tilt boundary migration coupled to shear deformation. *Acta Mater.* **55**, 1843–1848 (2007)
33. Mullins, W.W.: Two-dimensional motion of idealized grain boundaries. *J. Appl. Phys.* **27**, 900–904 (1956)
34. Qin, X.X., Gu, Y.J., Zhang, L.C., Xiang, Y.: Continuum model and numerical method for dislocation structure and energy of grain boundaries. *arXiv p. arXiv:2101.02596* (2021)
35. Rath, B.B., Winking, M., Li, J.C.M.: Coupling between grain growth and grain rotation. *Appl. Phys. Lett.* **90**, 161915 (2007)
36. Salvalaglio, M., Backofen, R., Elder, K., Voigt, A.: Defects at grain boundaries: A coarse-grained, three-dimensional description by the amplitude expansion of the phase-field crystal model. *Phys. Rev. Mater.* **2**, 053804 (2018)
37. Shewmon, P.G.: In: H. Margolin (ed.) *Recrystallization, grain growth and textures*, pp. 165–199. American Society of Metals, Metals Park (1966)
38. Srinivasan, S.G., Cahn, J.W.: Challenging some free-energy reduction criteria for grain growth. In: S. Ankem, C.S. Pande, I. Ovid'ko, S. Ranganathan (eds.) *Science and Technology of Interfaces*, pp. 3–14. TMS, Seattle (2002)
39. Sutton, A., Balluffi, R.: *Interfaces in Crystalline Materials*. Clarendon Press, Oxford (1995)
40. Taylor, J.E., Cahn, J.W.: Shape accommodation of a rotating embedded crystal via a new variational formulation. *Interfaces and Free Boundaries* **9**, 493–512 (2007)
41. Trautt, Z., Mishin, Y.: Grain boundary migration and grain rotation studied by molecular dynamics. *Acta Mater.* **60**, 2407–2424 (2012)
42. Upmanyu, M., Hassold, G.N., Kazaryan, A., Holm, E.A., Wang, Y., Patton, B., Srolovitz, D.J.: Boundary mobility and energy anisotropy effects on microstructural evolution during grain growth. *Interface Sci.* **10**, 201–216 (2002)
43. Upmanyu, M., Srolovitz, D.J., Lobkovsky, A.E., Warren, J.A., Carter, W.C.: Simultaneous grain boundary migration and grain rotation. *Acta Mater.* **54**, 1707–1719 (2006)
44. Wu, K.W., Voorhees, P.W.: Phase field crystal simulations of nanocrystalline grain growth in two dimensions. *Acta Mater.* **60**, 407–419 (2012)
45. Yamanaka, A., McReynolds, K., Voorhees, P.W.: Phase field crystal simulation of grain boundary motion, grain rotation and dislocation reactions in a bcc bicrystal. *Acta Mater.* **133**, 160–171 (2017)
46. Zhang, H., Upmanyu, M., Srolovitz, D.J.: Curvature driven grain boundary migration in aluminum: molecular dynamics simulations. *Acta Mater.* **53**, 79–86 (2005)
47. Zhang, J., Du, Q.: Numerical studies of discrete approximations to the Allen-Cahn equation in the sharp interface limit. *SIAM J. Sci. Comput.* **31**, 3042–3063 (2009)
48. Zhang, L., Xiang, Y.: A new formulation of coupling and sliding motions of grain boundaries based on dislocation structure. *SIAM J. Appl. Math.* **80**, 2365–2387 (2020)
49. Zhang, L.C., Gu, Y.J., Xiang, Y.: Energy of low angle grain boundaries based on continuum dislocation structure. *Acta Mater.* **126**, 11–24 (2017)
50. Zhang, L.C., Xiang, Y.: Motion of grain boundaries incorporating dislocation structure. *J. Mech. Phys. Solids* **117**, 157–178 (2018)
51. Zhu, X.H., Xiang, Y.: A continuum model for the dynamics of dislocation arrays. *Commun. Math. Sci.* **10**, 1081–1103 (2012)
52. Zhu, X.H., Xiang, Y.: Continuum framework for dislocation structure, energy and dynamics of dislocation arrays and low angle grain boundaries. *J. Mech. Phys. Solids* **69**, 175–194 (2014)

---

# A Three-Dimensional Continuum Simulation Method for Grain Boundary Motion Incorporating Dislocation Structure Supplementary Materials

Xiaoxue Qin · Luchan Zhang · Yang  
Xiang

## 1 Numerical simulations of bcc spherical grain boundaries with rotation axis [011]

In this section, we perform numerical simulations of grain boundary dynamics using our numerical algorithm presented in the main text.

Now we consider grain boundaries in bcc Fe. We choose the directions [100], [01 $\bar{1}$ ] and [011] to be the  $x$ ,  $y$  and  $z$  directions, respectively. There seven possible Burgers vectors, and in this coordinate system, they are  $\mathbf{b}^{(1)} = \left(\frac{1}{2}, 0, \frac{\sqrt{2}}{2}\right) a$ ,  $\mathbf{b}^{(2)} = \left(\frac{1}{2}, \frac{\sqrt{2}}{2}, 0\right) a$ ,  $\mathbf{b}^{(3)} = \left(\frac{1}{2}, -\frac{\sqrt{2}}{2}, 0\right) a$ ,  $\mathbf{b}^{(4)} = \left(-\frac{1}{2}, 0, \frac{\sqrt{2}}{2}\right) a$ ,  $\mathbf{b}^{(5)} = (1, 0, 0)a$ ,  $\mathbf{b}^{(6)} = \left(0, \frac{\sqrt{2}}{2}, \frac{\sqrt{2}}{2}\right) a$ , and  $\mathbf{b}^{(7)} = \left(0, -\frac{\sqrt{2}}{2}, \frac{\sqrt{2}}{2}\right) a$ , where  $a$  is the lattice constant. For bcc Fe,  $a = 0.2856\text{nm}$  and the Poisson ratio is  $\nu = 0.29$ . The rotation axis is  $\mathbf{a} = (0, 0, 1)$ , i.e., in the [011] direction.

We also study the evolution of an initially spherical grain boundary, whose radius is  $R = 20b$  and misorientation angle is  $\theta = 4^\circ$ . There are three sets of dislocations with Burgers vectors  $\mathbf{b}^{(2)}$ ,  $\mathbf{b}^{(3)}$ ,  $\mathbf{b}^{(5)}$ , respectively, in the equilibrium dislocation structure on this initial, spherical grain boundary; see the top image in Fig. 1(a). Parametrization and discretization of the grain boundary are the same as those for the grain boundary in fcc in the main text.

---

X. X. Qin  
Department of Mathematics, Hong Kong University of Science and Technology, Clear Water Bay, Kowloon, Hong Kong. E-mail: maxqin@ust.hk

L. C. Zhang  
College of Mathematics and Statistics, Shenzhen University, Shenzhen, 518060, China. Corresponding author. E-mail: zhanglc@szu.edu.cn

Y. Xiang  
Department of Mathematics, Hong Kong University of Science and Technology, Clear Water Bay, Kowloon, Hong Kong. Corresponding author. E-mail: maxiang@ust.hk

### 1.1 Pure coupling motion

We first consider the motion of this grain boundary without dislocation reaction, i.e. the reaction mobility  $M_r = 0$  in Eq. (54) (and Eq. (43)). This is the pure coupling motion.

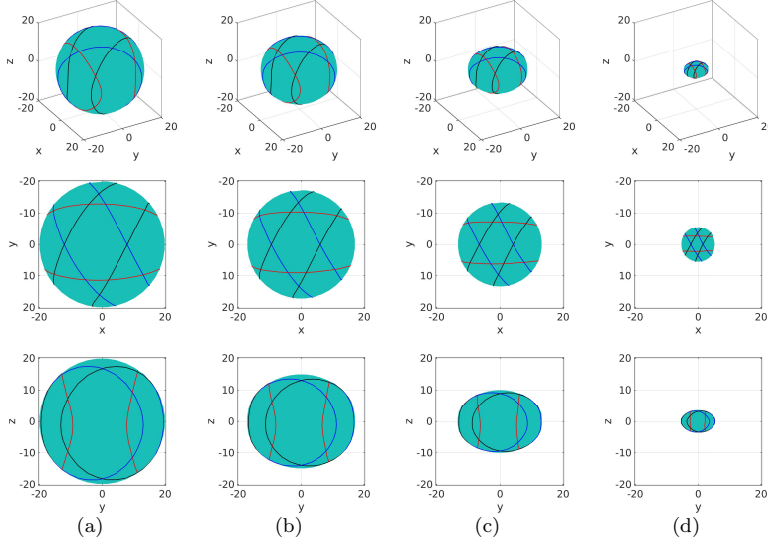


**Fig. 1** Shrinkage of an initially spherical grain boundary in bcc under pure coupling motion, i.e., without dislocation reaction. The rotation axis is the  $z$  direction ( $[011]$ ), and the initial misorientation angle  $\theta = 4^\circ$ . The upper panel of images show the three-dimensional view of the grain boundary during evolution. The middle panel of images show the grain boundary during evolution viewed from the  $+z$  direction ( $[011]$ ), and the lower panel of images show the grain boundary during evolution viewed from the  $+x$  direction ( $[100]$ ). Dislocations with Burgers vectors  $\mathbf{b}^{(2)}$ ,  $\mathbf{b}^{(3)}$  and  $\mathbf{b}^{(5)}$  are shown by blue, black and red lines, respectively. Length unit:  $b$ . (a) The initial spherical grain boundary. (b), (c), and (d) Configurations at time  $t = 3/M_d\mu$ ,  $6/M_d\mu$ ,  $9/M_d\mu$ , respectively.

Fig. 1 shows the shrinkage of this spherical grain boundary in bcc under the pure coupling motion. Evolutions of the grain boundary and its dislocation structure are similar to those of the grain boundary in fcc discussed in the main text. Especially, the shrinkage of the grain boundary is faster in the direction of the rotation axis than in other directions, which agrees with the results of atomistic simulations using phase field crystal models [5, 1]. Again, this anisotropic motion can be explained based on our continuum model by the constraint of Frank's formula in any direction normal to the rotation axis. The shape-preserving evolution of the equator of the grain boundary (with respect to the rotation axis) agrees with the results of the two-dimensional grain boundary dynamics models [2, 3, 4, 7, 6].



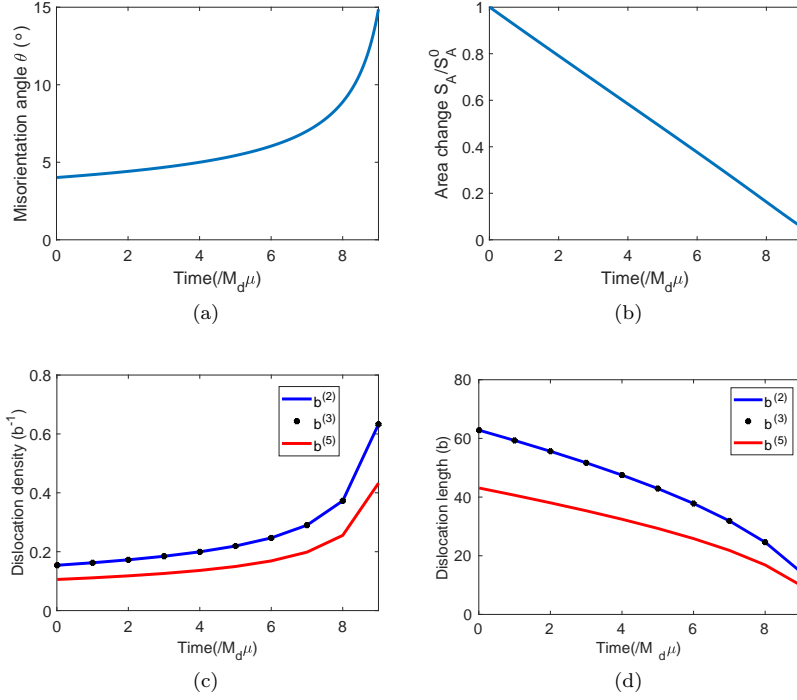


**Fig. 2** Shrinkage of an initially spherical grain boundary in bcc under pure coupling motion. The rotation axis is the  $z$  direction ( $[011]$ ), and the initial misorientation angle  $\theta = 4^\circ$ . (a) Evolution of misorientation angle  $\theta$ . (b) Evolution of grain boundary area  $S_A$ , where  $S_A^0$  is the area of the initial grain boundary. (c) Evolution of densities of dislocations on the grain boundary. These dislocations have Burgers vectors  $\mathbf{b}^{(2)}$ ,  $\mathbf{b}^{(3)}$ , and  $\mathbf{b}^{(5)}$  on the grain boundary. (d) Evolution of the total lengths of dislocations with these Burgers vectors. The densities and total lengths of dislocations with the Burgers vectors  $\mathbf{b}^{(2)}$ ,  $\mathbf{b}^{(3)}$ , and  $\mathbf{b}^{(5)}$  are shown by blue lines, black dots, and red lines, respectively, in (c) and (d).

Fig. 2 shows the increase of the misorientation angle  $\theta$ , linear decrease of the grain boundary area, increase of densities of dislocations, and decrease of the total lengths of dislocations during the shrinkage of the grain boundary. These results are similar to those of the grain boundary in fcc discussed in the main text and are consistent with available phase field crystal and two dimensional simulation results; see the discussion there. Note that for the dynamics of this grain boundary in bcc, the densities and total lengths of dislocations with Burgers vectors  $\mathbf{b}^{(2)}$  and  $\mathbf{b}^{(3)}$  are almost identical, and are greater than those of dislocations with Burgers vector  $\mathbf{b}^{(5)}$ . Recall that the lengths of Burgers vectors  $\mathbf{b}^{(2)}$  and  $\mathbf{b}^{(3)}$  are equal, and are smaller than the length of Burgers vector  $\mathbf{b}^{(5)}$ .

## 1.2 Motion with dislocation reaction

Now we perform simulations using our continuum model considering dislocation reaction, i.e.  $M_r \neq 0$ , for the motion of a grain boundary in bcc Fe. We use the same initial spherical grain boundary as in Sec. 1.1 without dislocation reaction.

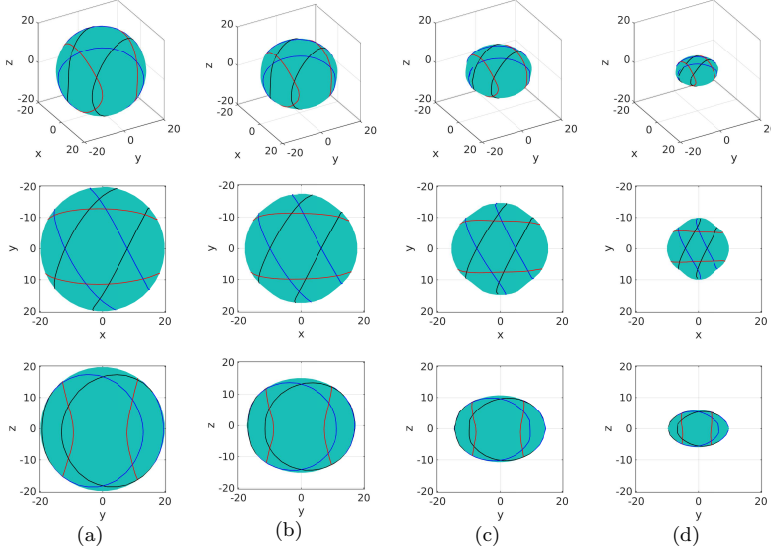


**Fig. 3** Shrinkage of an initially spherical grain boundary in bcc with dislocation reaction:  $M_r b^3 / M_d = 7.01 \times 10^{-5}$ . The rotation axis is the  $z$  direction ( $[011]$ ), and the initial misorientation angle  $\theta = 4^\circ$ . The upper panel of images show the three-dimensional view of the grain boundary during evolution. The middle panel of images show the grain boundary during evolution viewed from the  $+z$  direction ( $[011]$ ), and the lower panel of images show the grain boundary during evolution viewed from the  $+x$  direction ( $[100]$ ). Dislocations with Burgers vectors  $\mathbf{b}^{(2)}$ ,  $\mathbf{b}^{(3)}$  and  $\mathbf{b}^{(5)}$  are shown by blue, black and red lines, respectively. Length unit:  $b$ . (a) The initial spherical grain boundary. (b), (c), and (d) Configurations at time  $t = 3/M_d \mu, 6/M_d \mu, 9/M_d \mu$ , respectively.

Fig. 3 shows the shrinkage of the initially spherical grain boundary with dislocation reaction, where the reaction mobility  $M_r b^3 / M_d = 7.01 \times 10^{-5}$ . As in the evolution of the grain boundary in fcc with dislocation reaction shown in the main text, the equator of the grain boundary (with respect to the rotation axis) gradually evolves from a circle into a hexagon. However, unlike in fcc, here the grain boundary in bcc evolves into a non-regular hexagon. This is due to the fact that here the lengths of Burgers vectors  $\mathbf{b}^{(2)}$  and  $\mathbf{b}^{(3)}$  are smaller than the length of Burgers vector  $\mathbf{b}^{(5)}$ , while in the grain boundary in fcc, the three Burgers vectors have the same length. Again, we can see that the shrinkage of the grain boundary is faster in the direction of the rotation

axis than in other directions. These results agree with the those of phase field crystal simulations [5].

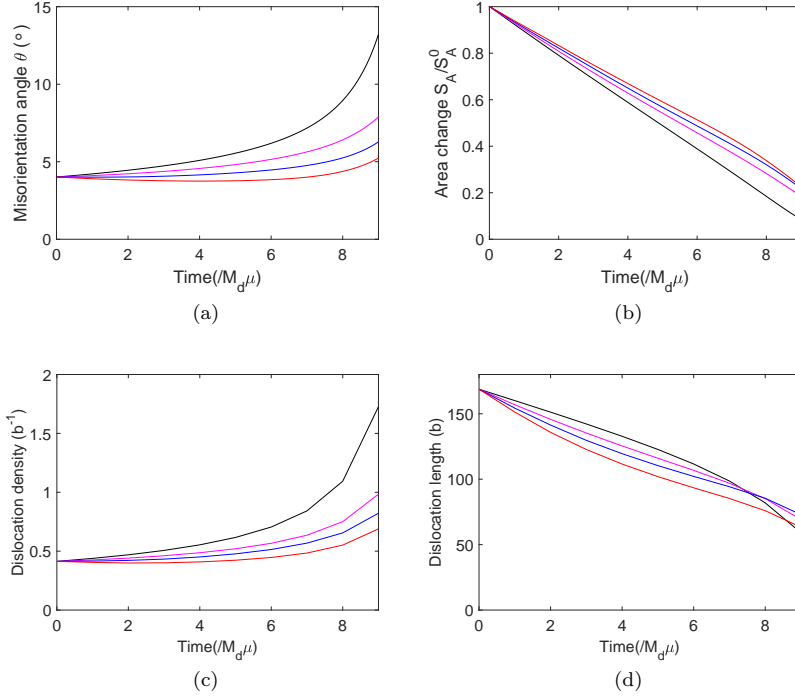


**Fig. 4** Shrinkage of an initially spherical grain boundary in bcc with different values of reaction mobility  $M_r$ . The rotation axis is the  $z$  direction ( $[011]$ ), and the initial misorientation angle  $\theta = 4^\circ$ . The reaction mobility  $M_r b^3/M_d = 0, 7.01 \times 10^{-5}, 1.40 \times 10^{-4}$ , and  $2.11 \times 10^{-4}$  from the top curve to the bottom one in (a), (c) and (d), and from the bottom to the top ones in (b). (a) Evolution of misorientation angle  $\theta$ . (b) Evolution of grain boundary area  $S_A$ , where  $S_A^0$  is the area of the initial grain boundary. (c) Evolution of the density of all the dislocations on the grain boundary. (d) Evolution of the total length of all the dislocations on the grain boundary.

Evolution of the misorientation angle  $\theta$  with different values of reaction mobility  $M_r$  is shown in Fig. 4(a). When  $M_r \neq 0$ , the evolution of misorientation angle is controlled by both the coupling effect (which is associated with the conservation of dislocations and increases  $\theta$ ) and sliding effect (which is associated with dislocation reaction and decreases  $\theta$ ). While the misorientation angle  $\theta$  is increasing during the evolution, the increase rate of  $\theta$  decreases as the dislocation reaction mobility  $M_r$  increases. Fig. 4(b) shows the evolution of grain boundary area with different values of dislocation reaction mobility  $M_r$ . The decrease of grain boundary area still follows the linear law in Eq. (62)

in the main text except in the later stage of the evolution with high dislocation reaction mobility, and is slower for higher dislocation reaction mobility. Figs. 4(c) and (d) show the evolutions of dislocation densities on the grain boundary and total length of dislocations with different values of reaction mobility  $M_r$ . The density of the dislocations on the grain boundary is increasing whereas the total length of dislocations is decreasing for these values of dislocation reaction mobility  $M_r$ . As the dislocation reaction mobility  $M_r$  increases, the increase rate of dislocation density decreases, and the decrease rate of the total length of dislocations increases except for the later stage of evolution without dislocation reaction. These behaviors are similar to those of the grain boundary in fcc shown in Fig. 5 in the main text, and more discussion can be found there. These results also agree with the available phase field crystal simulation results [5, 1].

## References

1. Salvalaglio, M., Backofen, R., Elder, K., Voigt, A.: Defects at grain boundaries: A coarse-grained, three-dimensional description by the amplitude expansion of the phase-field crystal model. *Phys. Rev. Mater.* **2**, 053804 (2018)
2. Srinivasan, S.G., Cahn, J.W.: Challenging some free-energy reduction criteria for grain growth. In: S. Anken, C.S. Pande, I. Ovid'ko, S. Ranganathan (eds.) *Science and Technology of Interfaces*, pp. 3–14. TMS, Seattle (2002)
3. Taylor, J.E., Cahn, J.W.: Shape accommodation of a rotating embedded crystal via a new variational formulation. *Interfaces and Free Boundaries* **9**, 493–512 (2007)
4. Wu, K.W., Voorhees, P.W.: Phase field crystal simulations of nanocrystalline grain growth in two dimensions. *Acta Mater.* **60**, 407–419 (2012)
5. Yamanaka, A., McReynolds, K., Voorhees, P.W.: Phase field crystal simulation of grain boundary motion, grain rotation and dislocation reactions in a bcc bicrystal. *Acta Mater.* **133**, 160–171 (2017)
6. Zhang, L., Xiang, Y.: A new formulation of coupling and sliding motions of grain boundaries based on dislocation structure. *SIAM J. Appl. Math.* **80**, 2365–2387 (2020)
7. Zhang, L.C., Xiang, Y.: Motion of grain boundaries incorporating dislocation structure. *J. Mech. Phys. Solids* **117**, 157–178 (2018)